



**HAL**  
open science

## Global climate modelling of Saturn's atmosphere, Part V: Large-scale vortices

Padraig T Donnelly, Aymeric Spiga, Sandrine Guerlet, Matt K James,  
Deborah Bardet

### ► To cite this version:

Padraig T Donnelly, Aymeric Spiga, Sandrine Guerlet, Matt K James, Deborah Bardet. Global climate modelling of Saturn's atmosphere, Part V: Large-scale vortices. *Icarus*, In press, pp.116302. 10.1016/j.icarus.2024.116302 . insu-04694942v1

**HAL Id: insu-04694942**

**<https://insu.hal.science/insu-04694942v1>**

Submitted on 11 Sep 2024 (v1), last revised 13 Sep 2024 (v2)

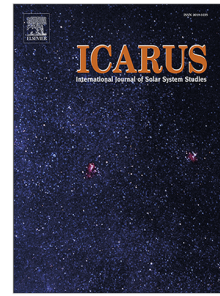
**HAL** is a multi-disciplinary open access archive for the deposit and dissemination of scientific research documents, whether they are published or not. The documents may come from teaching and research institutions in France or abroad, or from public or private research centers.

L'archive ouverte pluridisciplinaire **HAL**, est destinée au dépôt et à la diffusion de documents scientifiques de niveau recherche, publiés ou non, émanant des établissements d'enseignement et de recherche français ou étrangers, des laboratoires publics ou privés.

## Journal Pre-proof

Global climate modelling of Saturn's atmosphere, Part V: Large-scale vortices

Padraig T. Donnelly, Aymeric Spiga, Sandrine Guerlet, Matt K. James, Deborah Bardet



PII: S0019-1035(24)00362-2  
DOI: <https://doi.org/10.1016/j.icarus.2024.116302>  
Reference: YICAR 116302

To appear in: *Icarus*

Received date: 10 April 2024  
Revised date: 3 September 2024  
Accepted date: 4 September 2024

Please cite this article as: P.T. Donnelly, A. Spiga, S. Guerlet et al., Global climate modelling of Saturn's atmosphere, Part V: Large-scale vortices. *Icarus* (2024), doi: <https://doi.org/10.1016/j.icarus.2024.116302>.

This is a PDF file of an article that has undergone enhancements after acceptance, such as the addition of a cover page and metadata, and formatting for readability, but it is not yet the definitive version of record. This version will undergo additional copyediting, typesetting and review before it is published in its final form, but we are providing this version to give early visibility of the article. Please note that, during the production process, errors may be discovered which could affect the content, and all legal disclaimers that apply to the journal pertain.

© 2024 Published by Elsevier Inc.

# Global Climate Modelling of Saturn's Atmosphere

## Part V: Large-scale Vortices.

Padraig T. Donnelly<sup>a,b,\*</sup>, Aymeric Spiga<sup>b,c</sup>, Sandrine Guerlet<sup>b,d</sup>, Matt K. James<sup>e</sup>, Deborah Bardet<sup>e</sup>

<sup>a</sup>Laboratoire Atmosphères, Milieux, Observations Spatiales / Institut Pierre-Simon Laplace (LATMOS/IPSL), Sorbonne Université, Centre National de la Recherche Scientifique (CNRS), École Polytechnique, École Normale Supérieure (ENS), address: Campus Pierre et Marie Curie BC99, 4 place Jussieu, 75005 Paris, France

<sup>b</sup>Laboratoire de Météorologie Dynamique / Institut Pierre-Simon Laplace (LMD/IPSL), Sorbonne Université, Centre National de la Recherche Scientifique (CNRS), École Polytechnique, École Normale Supérieure (ENS), address: Campus Pierre et Marie Curie BC99, 4 place Jussieu, 75005 Paris, France

<sup>c</sup>Institut Universitaire de France (IUF), address: 1 rue Descartes, 75005 Paris, France

<sup>d</sup>LESIA, Observatoire de Paris, Université PSL, CNRS, Sorbonne Université, Univ. Paris Diderot, Sorbonne Paris Cité, address: 5 place Jules Janssen, 92195 Meudon, France.

<sup>e</sup>University of Leicester, address: University of Leicester, University Road, Leicester, LE1 7RH, UK

---

### Abstract

This paper presents an analysis of large-scale vortices in the atmospheres of gas giants, focusing on a detailed study conducted using the Saturn-DYNAMICO global climate model (GCM). Large-scale vortices, a prominent feature of gas giant atmospheres, play a critical role in their atmospheric dynamics. By employing three distinct methods—manual detection, machine learning via artificial neural networks (ANN), and dynamical detection using the Automated Eddy-Detection Algorithm (AMEDA)—we characterize the spatial, temporal, and dynamical properties of these vortices within the Saturn-DYNAMICO GCM. Our findings reveal a consistent production of vortices due to well-resolved eddy-to-mean flow interactions, exhibiting size and intensity distributions broadly in agreement with observational data. However, notable differences in vortex location, size, and concentration highlight the model's limitations and suggest areas for further refinement. The analysis underscores the

---

\*Corresponding author: padraig.donnelly@latmos.ipsl.fr

importance of zonal wind conditions in influencing vortex characteristics and suggests that more accurate modelling of giant planet vortices may require improved representation of moist convection and jet structure. This study not only provides insights into the dynamics of Saturn's atmosphere as simulated by the GCM but also offers a framework for comparing vortex characteristics across observations and models of planetary atmospheres.

*Keywords:* Gas giants, Saturn, Vortices, Global climate model, Eddy-to-mean flow interactions, Geospatial Information Systems, Machine learning, Dynamical detection, Atmospheric dynamics.

---

## 1. Introduction

A general feature of planetary atmospheres is the presence of strong zonal flows that arise from thermal gradients and planetary rotation effects. The complex interaction between eddy momentum fluxes and these zonal jets can often give rise to intense shears and retrograde flows which can lead to vortical structures. These dynamically-closed features are found in many planetary atmospheres.

Vortices are ubiquitous on Jupiter, with a great deal of variability in spatial structure and lifetime between the largely cool and cloudy white anticyclones to the warm and volatile-rich dark cyclones (Smith et al., 1979; Ingersoll et al., 1979; Mitchell et al., 1979; Rogers, 1995; Vasavada et al., 1998; Fletcher et al., 2022; Orton et al., 2022). Jovian anticyclones are often more long-lived than their cyclonic counterparts, sometimes existing for many years, compared to the often transient cyclones. Cyclones are generally fewer in number and potentially far more irregular in shape, sometimes being quite zonally-oblate (Morales-Juberias et al., 2002; Legarreta and Sánchez-Lavega, 2005). Jovian cyclones and anticyclones typically form in their associated region of shear with vorticity magnitudes on the order of the planetary and local wind shear vorticities (Mac Low and Ingersoll, 1986; Legarreta and Sánchez-Lavega, 2005). Recent observations from the NASA Juno spacecraft reveal complex, stable configurations

21 of circumpolar cyclones, of a kind that are not observed on other giant planets  
22 (Orton et al., 2017; Adriani et al., 2018).

23 The atmosphere of Saturn exhibits fewer discrete vortices than Jupiter.  
24 Prominent anticyclonic white ovals have been observed from the Pic-du-Midi  
25 Observatory (Sánchez-Lavega et al., 1997), and by the Voyager (Smith et al.,  
26 1981; Smith et al., 1982; García-Melendo et al., 2007) and Cassini (Vasavada  
27 et al., 2006; Trammell et al., 2014, 2016) [spacecraft](#), sometimes lasting for years  
28 and experiencing merging events with smaller spots. There is a relative dearth  
29 of stable cyclonic spots on Saturn, with the most notable being the long-lived  
30 and UV-bright spot observed from the ground (Sánchez-Lavega et al., 2000),  
31 by Voyager 2 (Smith et al., 1982), and by the Hubble Space Telescope (HST,  
32 Caldwell et al., 1993). Cassini also observed the long-lived southern cyclone at  
33  $\sim 46^\circ\text{S}$  (del Río-Gaztelurrutia et al., 2010), groups of vortices like the relatively  
34 long-lived cyclone-anticyclone coupled system at  $\sim 59^\circ\text{N}$  (del Río-Gaztelurrutia  
35 et al., 2018), the long chain of infrared-bright spots at  $\sim 33^\circ\text{N}$  (the “String of  
36 Pearls”, Sayanagi et al., 2014), and the dark ovals frequently generated in a  
37 region of vigorous convection, thunderstorm, and lightning activity at  $33\text{-}39^\circ\text{N}$   
38 (“Storm Alley” Sromovsky et al., 2018). There has been extensive study of  
39 the polar region from ground-based (Orton and Yanamandra-Fisher, 2005) and  
40 space-based (Sánchez-Lavega et al., 2006; Dyudina et al., 2008; Fletcher et al.,  
41 2008; Dyudina et al., 2009; Baines et al., 2009; Antuñano et al., 2015; Sayanagi  
42 et al., 2017; Antuñano et al., 2018) observatories, revealing a circular stable cy-  
43 clone at each pole. This structure is analogous to the polar cyclones on Jupiter  
44 and [is](#) expected to be common on the gas giants (O’Neill et al., 2015; Scott,  
45 2011).

46 On Uranus, ground-based and spacecraft observations (Sromovsky et al.,  
47 2012) present a dominant view of clouds exhibiting many small bright spots (po-  
48 tentially regions featuring cumulus-like convection) with associated dark spots.  
49 Further ground-based observations (de Pater et al., 2015) detected near-infrared-  
50 bright, rapidly-evolving, discrete cloud features that suggest more structured  
51 vortical systems deeper in the atmosphere.

52 On Neptune, the historical record contains two prominent anticyclones im-  
53 aged by Voyager (Smith et al., 1989; Limaye and Sromovsky, 1991; Sromovsky  
54 et al., 1993). Ground-based observations detected a large circumpolar prograde  
55 jet at approximately 80 °S surrounding an infrared-bright polar region (Luszcz-  
56 Cook et al., 2010). These highest southern latitudes exhibit large-scale subsi-  
57 dence, warming, slowing of the peripheral jet, and potential volatile depletion,  
58 suggestive of cyclonic motion (Fletcher et al., 2014).

59 Large-scale vortices are key to understand the atmospheric dynamics on  
60 gas giants (Sada et al., 1996; Simon-Miller et al., 2002; Ingersoll et al., 2004;  
61 Vasavada and Showman, 2005; del Genio et al., 2009), providing insights into  
62 the vertical structure and sources of forcing for long-lived stable features (e.g.  
63 zonal jets) and ephemeral convective events (e.g. moist convective outbreaks).  
64 Therefore, it is crucial to also consider theoretical models (e.g. radiative, chem-  
65 ical, and dynamical) to enrich knowledge of vortices and large-scale dynamics  
66 gained from observations (Ingersoll et al., 1981; Williams and Yamagata, 1984;  
67 Dowling and Ingersoll, 1989; Marcus et al., 2000; Li et al., 2006; Showman, 2007;  
68 del Río-Gaztelurrutia et al., 2010; Rostami et al., 2017).

69 In recent years there has been much study into idealised and comprehen-  
70 sive numerical models to investigate large-scale dynamics. A significant chal-  
71 lenge in gas giant modelling is representing the depth and forcing of large-scale  
72 dynamics. As a result, two approaches have emerged to investigate the tro-  
73 pospheric dynamics on the giant planets. One is the “shallow-forcing” model  
74 which uses equations that assume a thin atmosphere to capture weather-layer  
75 phenomena like baroclinic instability and moist convective storms (Vasavada  
76 and Showman, 2005; Lian and Showman, 2008; Schneider and Liu, 2009; Liu  
77 and Schneider, 2010; Lian and Showman, 2010; García-Melendo et al., 2010).  
78 The other is the “deep-seated” dynamo-like model that captures convection  
79 through the planet’s molecular envelope (Heimpel et al., 2005; Yano et al.,  
80 2005; Kaspi et al., 2009; Heimpel and Gómez Pérez, 2011; Gastine et al., 2014;  
81 Heimpel et al., 2016; Cabanes et al., 2017). The shallow weather-layer mod-  
82 els, like the Saturn-DYNAMICO GCM described in this paper, reproduce well

83 convective events, large-scale vortices, and high-latitude westward jets, and the  
84 deep-seated models reproduce the strength and stability of the equatorial super-  
85 rotating zonal jet, but the challenge remains to capture all of these phenomena  
86 under a single scheme (Vasavada and Showman, 2005; Lian and Showman, 2008;  
87 Schneider and Liu, 2009; Liu and Schneider, 2010; Lian and Showman, 2010;  
88 García-Melendo et al., 2010). However, recent observational studies have shown  
89 that jets are much deeper than the vertical extent of shallow-water models, but  
90 shallower than what some deep models assume (Kaspi et al., 2018; Guillot et al.,  
91 2018; Galanti et al., 2019), implying merits to each methodology for modelling  
92 large-scale dynamics.

93 Despite the many observations of giant planet vortices, it remains a  
94 challenge to perform a comprehensive long-term study of the statistical  
95 morphologies and dynamics of vortices. Amateur visible-light and near-IR  
96 data continues to provide an invaluable scientific tool for vortex classification  
97 (Rogers, 1995; Rogers et al., 2006; Inurrigarro et al., 2020; Hueso et al., 2022),  
98 and the NASA Juno spacecraft has enabled unprecedented opportunity to clas-  
99 sify the jovian polar and circumpolar vortices (Adriani et al., 2018; Grassi et al.,  
100 2018; Kaspi et al., 2018; Adriani et al., 2020; Li et al., 2020; Tabataba-Vakili  
101 et al., 2020; Bolton et al., 2021; Scarica et al., 2022; Siegelman et al., 2022a,b).  
102 For Saturn, the natural differences in vortex appearance and the relatively  
103 lower spatial resolution of amateur observations makes comparable study on  
104 Saturn difficult, despite decades of observations from ground-based (Hanel  
105 et al., 1981, 1982; Fletcher et al., 2009; Blake et al., 2023) and space-based  
106 (Karkoschka and Tomasko, 2005; Pérez-Hoyos et al., 2005; Fletcher et al., 2023)  
107 observatories.

108 Until recently there has not been a fully eddy-resolved, multi-year global  
109 circulation model of the gas giants that manifests cloud-top vortices without  
110 forcing or parameterisation. The Saturn-DYNAMICO GCM presents a unique  
111 opportunity to explore the eddy-driven production of vortices from eddy-jet  
112 interaction in the context of a Saturn-like planet (see Section 2). Long-lived,  
113 large-scale vortices occur spontaneously in the model, but so far they have

114 not been studied in detail. This work characterises the spatial, temporal, and  
115 dynamical structure of these vortices over multiple Saturn years. With the  
116 wealth of vortices in the model and the benefits of direct dynamical outputs,  
117 we explore three different detection methodologies and compare the results to  
118 previous observational studies of vortices on Saturn.

119 We briefly introduce the reference simulation from Saturn-DYNAMICO  
120 GCM in Section 2.1 and the general approach to the detection of large-scale  
121 vortices on the giant planets in Section 2.2. In Sections 2.3, 2.4, and 2.5 we  
122 introduce the three vortex detection methodologies used in this comparative  
123 analysis. Section 3 compares the statistical distributions of model parameters  
124 for all vortices detected by the three methods, with a focus on spatial and tem-  
125 poral distributions, vortex size, vortex shape, and local wind conditions. Finally,  
126 Section 4 discusses the model vortices in the context of observational studies of  
127 the giant planets, reflects on the strengths and limitations of the three methods  
128 for vortex detection, and discusses implications for future study.

## 129 2. Methodology

### 130 2.1. Saturn-DYNAMICO Global Climate Model

131 The Saturn-DYNAMICO GCM is comprised of a radiative-seasonal model  
132 coupled to a hydrodynamical core that solves the shallow-layer equations on  
133 an icosahedral grid, with 32 atmospheric layers from 1-3000 mbar (Spiga et al.,  
134 2020). The model is optimised for massively-parallel computation which has en-  
135 abled the high-resolution numerical simulation of Saturn’s atmosphere on a half-  
136 degree latitude-longitude grid for fifteen modelled planetary years. Radiative  
137 transfer modelling uses correlated- $k$  distributions based on HITRAN line data  
138 for the primary hydrocarbons ( $\text{CH}_4$ ,  $\text{C}_2\text{H}_6$ , and  $\text{C}_2\text{H}_2$ , Rothman et al., 2013),  
139 collision-induced absorption from  $\text{H}_2$ - $\text{H}_2$ ,  $\text{H}_2$ -He, tropospheric and stratospheric  
140 aerosols, as well as ring shadowing effects and internal heat fluxes (Guerlet et al.,  
141 2014). Along with an internal heat flux, the model has a Rayleigh-like drag layer  
142 at the model bottom, which emulates the deep zonal flows and which acts to



143 close the angular momentum budget. Initial winds are set to zero with a single  
144 vertical profile of temperature everywhere, and the model has sufficient spatial  
145 resolution to directly resolve the eddy-to-mean energy cascade over the long  
146 spin-up time of eight years to achieve steady-state flow (Cabanes et al., 2020).  
147 This steady state from model year eight to fifteen in Spiga et al. (2020) forms  
148 the data set for this work (discussed in Section 2.2).

149 The steady-state Saturn-DYNAMICO model produces a thermal structure  
150 consistent with Cassini/CIRS measurements of Saturn (Spiga et al., 2020),  
151 as well as a realistic zonal jet structure (except for the super-rotating equa-  
152 torial jet, largely underestimated in the simulation), eddy-acceleration of the  
153 jets, and atmospheric planetary-scale waves. Subsequent studies using Saturn-  
154 DYNAMICO have explored the inverse cascade giving rise to jets (Cabanes  
155 et al., 2020), the stratospheric equatorial dynamics and their impact on the  
156 quasi-periodic equatorial oscillation (Bardet et al., 2021), and the impact of  
157 moist convection on zonal dynamics in the Jupiter configuration (Boissinot et al.,  
158 2024).

159 These eddy-driven dynamics also give rise to quasi-periodic “eddy-burst  
160 events”, wherein small-scale instabilities accumulate to cause abrupt stochastic  
161 transitions in the zonal jet structure (Bouchet and Simonnet, 2009; Bouchet  
162 et al., 2013). During these events the zonal flow is disrupted on a global scale,  
163 rapidly transporting momentum and accelerating the zonal jets. These eddy-  
164 burst events are qualitatively similar to the large-scale upheavals observed on  
165 Jupiter (Rogers, 1995; Fletcher et al., 2011; Pérez-Hoyos et al., 2012; Sánchez-  
166 Lavega et al., 2017; Fletcher et al., 2017a,b), albeit markedly more intense and  
167 distributed. A particular event of interest is the one seen in Figure 1. These  
168 events happen sporadically in both hemispheres, but during this event the north-  
169 ern hemisphere remained relatively quiescent, with a growing instability from  
170 the jet-vortex interaction on the northern edge of the prominent southern cy-  
171 clone at  $\sim 75^\circ\text{S}$ . The early quiescent stage (Figure 1a) is marked by slowly-  
172 varying zonal jets and a near-constant background vorticity structure on the  
173 timescales considered here. The disturbed stage (Figure 1b) is dominated by

174 intense horizontal shear and disruption of the zonal mean state. The final stage  
175 (Figure 1c) is a period of relaxation back to the quiescent state wherein the  
176 stable vortices merge over time and deposit their vorticity back into the mean  
177 flow via the zonal jets. We note here that while observational studies of Jupiter  
178 and Saturn discussed in this paper are typically from the low and mid latitudes,  
179 the vortices analysed in this study are exclusively from the polar region, for  
180 reasons discussed in Section 3.3.

## 181 2.2. Vortex detection - general approach

182 The choice of vortex detection method depends on the nature of the  
183 dataset. Sparse datasets of inconsistently-sampled imaging observations and  
184 continuously-modelled dynamical fields both present unique challenges. In this  
185 work, we treat the seven years of steady-state DYNAMICO model outputs as  
186 a “synthetic” observational dataset, which presents the opportunity to explore  
187 three distinct methods: visual detection and manual selection in images (previ-  
188 ous studies of gas giant vortices, [Li et al., 2004](#); [Vasavada et al., 2006](#); [Trammell  
189 et al., 2014, 2016](#)), a neural network trained by that approach, and a purely  
190 dynamical approach developed for terrestrial oceanic eddies based on modelled  
191 dynamical fields ([Le Vu et al., 2018](#)). This study explores the advantages and  
192 disadvantages of each approach, and quantifies the uncertainties and sensitiv-  
193 ities associated with each, with the ultimate goal to study large-scale vortices  
194 on Saturn.

195 This analysis utilises the Saturn-DYNAMICO GCM simulations of [Spiga  
196 et al. \(2020\)](#) to probe directly the thermal and dynamical signature of the  
197 large-scale vortices (Section 2.1). We assume that the 700-mbar model level  
198 corresponds approximately to Saturn’s cloud top and provides a meaningful  
199 comparison to the cloud-tracked aerosol populations of visible-light observations  
200 ([Li et al., 2004](#); [Vasavada et al., 2006](#); [Trammell et al., 2014, 2016](#); [Fletcher et al., 2023](#))  
201 . Despite small differences in wind fields between levels, there is no particular  
202 sensitivity to this assumption since the modeled troposphere in Saturn-  
203 DYNAMICO is fairly barotropic and large-scale tropospheric features can

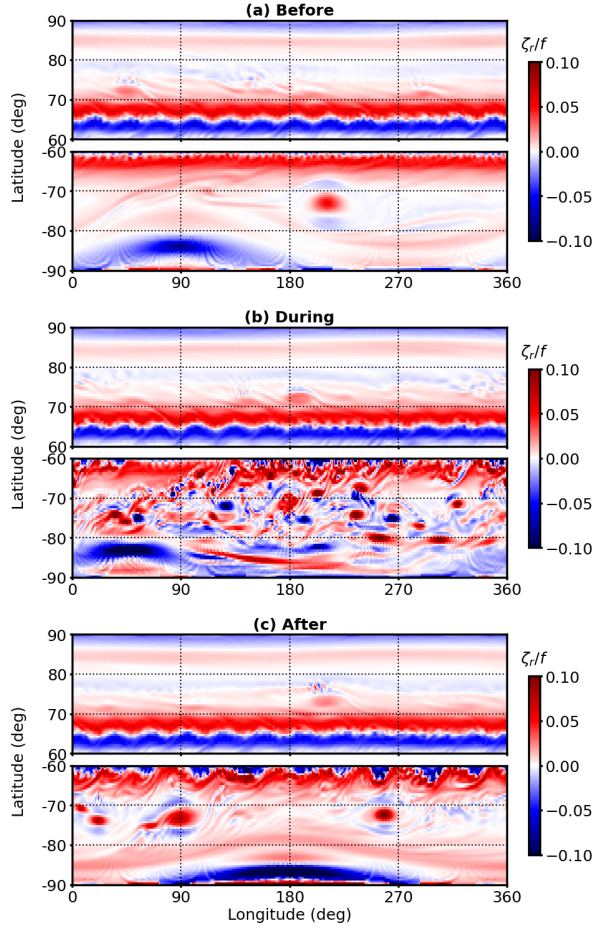


Figure 1: Relative vorticity field at 700 mbar from the Saturn-DYNAMICO GCM. Time lapse of 1000 model days from the beginning of model year 12 showing the stages before, during, and after a typical eddy-burst event. Vortex merging can be seen with two pairs of clockwise-orbiting cyclones in the southern 0-90° quadrant.

204 persist over many vertical levels. DYNAMICO currently uses a latitudinally-  
 205 uniform aerosol layer (necessary for radiative balance) and does not resolve  
 206 cloud microphysics, which renders these results insensitive to aerosol variations.

207 The three methods produce distributions of vortex location and size (on a  
 208 latitude-longitude grid). The angular geometry is then converted to geodesic

209 distances on a Saturn-like ellipsoid using the Karney formula for an ellipsoid  
 210 (Karney, 2012). This is necessary because DYNAMICO assumes a spherical ge-  
 211 ometry but Saturn is ellipsoidal. The oblateness of Saturn means that spherical  
 212 geodesic distances can diverge up to 20% zonally and 15% meridionally from  
 213 the Saturn ellipsoidal case. At each vortex centre we extract temperature,  $T$ ,  
 214 zonal wind,  $U$ , and meridional wind,  $V$ , which are direct outputs of the model  
 215 and used to calculate higher-order dynamical fields.

216 In the context of planetary atmospheres and oceanography, the Okubo-Weiss  
 217 parameter,  $W$ , defined in Equation 1, is a critical tool for distinguishing between  
 218 rotational and strain-dominated regions within a fluid flow (Okubo, 1970; Weiss,  
 219 1991). It has been used extensively to study coherent mesoscale eddies in the  
 220 terrestrial ocean (Isern-Fontanet et al., 2003; Morrow et al., 2004; Chelton et al.,  
 221 2007; Chaigneau et al., 2008), and is useful when discussing eddy growth, cyclo-  
 222 genesis and vortex development (merging and splitting) in giant planet atmo-  
 223 spheres. By applying the Okubo-Weiss parameter to the DYNAMICO model  
 224 outputs, we can gain deeper insights into the dynamical behavior of large-scale  
 225 cyclones and anticyclones in the Saturn-DYNAMICO GCM, and derive useful  
 226 diagnostic tools for analysis of vortices in planetary atmospheres.

$$W = \sigma_n^2 + \sigma_s^2 - \zeta_r^2, \quad (1)$$

227 where  $\sigma_n = u_x - v_y$ ,  $\sigma_s = v_x + u_y$ , and  $\zeta_r = v_x - u_y$  are the *shearing de-*  
 228 *formation rate*, the *straining deformation rate*, and the vertical component of  
 229 *relative vorticity*, respectively, where  $x$  represents the longitudinal distance and  
 230  $y$  represents the latitudinal distance. Using this parameter, we explore how the  
 231 diagnostic metrics developed for the study of submesoscale eddies in the terres-  
 232 trial ocean (Scherbina et al., 2013; Balwada et al., 2021) can be applied to the  
 233 interior of GCM the vortices to understand the dynamics close to the vortex  
 234 core. For comparison to these oceanographic studies we calculate the *horizontal*  
 235 *divergence*,  $\delta$ , where:

$$\delta = u_x + v_y, \quad (2)$$

236 and combine the two deformation terms into the *lateral strain rate*,  $\alpha$ , where:

$$\alpha = \sqrt{\sigma_n^2 + \sigma_s^2} \quad (3)$$

237 The  $W$  parameter is used in the dynamical approach detection step (Le Vu  
238 et al., 2018) and later its components are used to characterise the distribution  
239 of vortex dynamics (Section 3).

240 A direct assumption of the manual method (and an indirect one for the  
241 neural network) is that a vorticity feature is deemed to be a “vortex” if it has  
242 a circular or oval shape with a distinct vorticity magnitude and can be the  
243 same or opposite sign to the surrounding flow. This excludes short-lived eddies  
244 that are often the progenitors of longer-lived, stable vortices (see Section 2.1), as  
245 well as other eddy-dominated circulations like folded filamentary regions (FFRs,  
246 Rogers, 1995; Rogers et al., 2006; Wong et al., 2020; Fletcher et al., 2022), and  
247 convective/rifted regions.

248 Vasavada et al. (2006) suggest that the vorticity of each vortex is correlated  
249 to the vorticity of the surrounding zonal winds. They admit that they did not  
250 measure tangential velocities, and only approximately determined the vorticity  
251 sign based on observed behavior (e.g. orbiting and stability in surrounding shear  
252 zone), so it is conceivable that they did not correctly estimate all vorticities  
253 in that study. This limitation persists in the assumption of Trammell et al.  
254 (2014) that vortices in cyclonic shear regions are themselves cyclonic and vice-  
255 versa, though they also admit that this is not necessarily the case (as discussed  
256 in Section 3). This is a useful assumption due to the challenges associated  
257 with visible-light imaging of aerosol populations but it is not required in the  
258 present work using modelled dynamical fields. It is true that these fields used  
259 in this work are insensitive to the differences in vortex appearance caused by  
260 variations in cloud-top aerosols, so we cannot classify vortices in the same way  
261 as Vasavada et al. (2006); Trammell et al. (2014, 2016). However, they do

262 provide the opportunity to probe the dynamical field directly to find opposite-  
263 sign vortices, something that is not possible under the assumption of same-sign  
264 selection.

265 Observed vortices generally exhibit a fairly distinct bright or dark aerosol  
266 population embedded in a comparatively uniform bright background. Modelled  
267 vortices behave similarly and should naturally overlap with this kind of ob-  
268 servation being a roughly distinct vorticity feature in a comparatively uniform  
269 background shear. We assume that the edge of an observed and modelled vor-  
270 tex is the boundary within which all of the vorticity of the vortex is contained.  
271 Therefore, although not strictly the same, a modelled vortex does provide a  
272 good comparison to the observations in this analysis.

273 However, at smaller spatial scales it becomes difficult to distinguish between  
274 small, circular vortices and more ambiguous vorticity features that may be small-  
275 scale eddies or transient vortices. We observe the same lower bound of vortex  
276 size as the observational studies (discussed in Section 3), but our spatial resolu-  
277 tions differ; 100-150 km/pixel (Cassini/ISS) and 10-526 km/grid point (Saturn-  
278 DYNAMICO GCM from pole to equator at half-degree resolution), respectively.  
279 This means that we effectively have reduced spatial resolution at low-latitudes,  
280 and could be missing the smallest vortices that might be comparable to those in  
281 the data. The conclusion is that all model vortices would be visible in the ob-  
282 servations, but not all observed vortices are necessarily detectable in the model  
283 under these assumptions, so caution is needed when making direct comparisons.

### 284 *2.3. Manual detection - visual mapping*

285 The “synthetic data” used for the manual detection method use the rela-  
286 tive vorticity field,  $\zeta_r$ . This is comparable to the high-pass filtered images of  
287 (Vasavada et al., 2006; Trammell et al., 2014, 2016) since applying a high-pass  
288 filter often explicitly involves a similar subtraction of two-dimensional gradients.  
289 We tested similar maps of potential vorticity calculated on isentropes (lines of  
290 constant potential temperature) where maxima in vorticity are generally more  
291 distinct, but they offer no notable improvement on vortex detection at the cost

292 of increased computation.

293 Of the methods explored in this work, the manual vortex detection is the  
294 most direct comparator to observational studies. The model outputs are sam-  
295 pled at each solstice and equinox for seven modelled Saturn years. Later this  
296 count will be computed as a seasonal average for comparison to the other two  
297 methodologies (which have higher temporal sampling). Seasonal average here is  
298 defined as the simple mean of the vortex count in all model time steps in a bin of  
299 length one season (90 degrees of solar longitude) and centred on the solstice/e-  
300 quinox of a given season. This temporal sampling and similar fundamental  
301 measurement assumptions are intended to represent a “best-case” simulation  
302 of what could be expected from long-term giant planet observations. Maps  
303 are analysed using the free and open-source Quantum Geographic Information  
304 System (QGIS, [QGIS Development Team, 2022](#)) to measure features on the vor-  
305 ticity maps by visually identifying the vortex centre and overlaying a “ghost”  
306 ellipse until the vortex edge is considered to be completely enclosed. Since the  
307 vorticity map is inspected visually, there is notable sensitivity of the output to  
308 the contrast of values perceived by the human eye.

309 To constrain this sensitivity, ten prominent vortices were measured each at  
310 five magnifications and four map contrast modes, to estimate the uncertainty in  
311 vortex edge detection given that changing gradients can change the shape and  
312 size of the boundary. Figure 2 shows the measured uncertainties as well as the  
313 relative contribution of each map mode to the uncertainty. Using average values  
314 of the inter-quartile range (IQR), uncertainty in vortex latitude and longitude is  
315 approximately 0.1 and 0.2 %, respectively. The zonal and meridional diameters  
316 ( $D_x$  and  $D_y$ , respectively) are each on average  $\sim 10\%$ . The uncertainty in zonal  
317 and meridional diameters reaches a maximum of 60% in extreme cases where the  
318 vorticity gradient across the rim is small (i.e. weak vortex or strong background  
319 flow) or where there is significant spatial distortion from the cylindrical map  
320 projection (at the highest polar latitudes). It was found that the magnification  
321 of the map contributes more uncertainty (up to up to 50% more) than the  
322 contrast of the map.

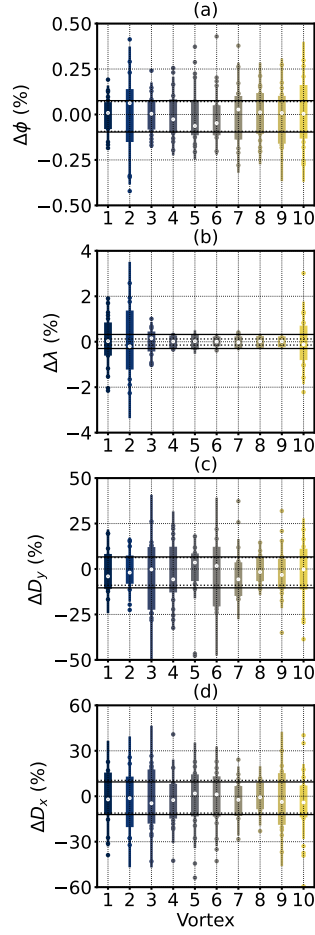


Figure 2: Measurement uncertainty for the manual vortex detection method showing central latitude and longitude (first and second rows, respectively) and meridional and zonal diameter (third and fourth rows, respectively) for each of 10 prominent model vortices obtained across 20 map configurations. Direct measurements are expressed as a percentage about the mean value for each vortex (coloured points), with the median value (white points), IQR (thick line), and upper and lower quartiles extended by the IQR (thin line). The degree to which the white points vary about zero represents the asymmetry of each distribution. Horizontal lines show the mean (thick) and median (dashed) quartile values.



323 *2.4. Machine learning - artificial neural network*

324 We utilise an Artificial Neural Network (ANN) to search for vortex-like fea-  
325 tures in the DYNAMICO model outputs, and use the results of the manual study  
326 as the training set for this algorithm. This approach is intended to implement  
327 the manual method in a more scalable and efficient way.

328 *2.4.1. Network Training*

329 To prepare the manually-detected vortices for input into the neural network,  
330 the DYNAMICO model fields are sub-sampled according to the spatial bounds  
331 of those vortices and down-sampled onto a  $6 \times 6$ -point latitude-longitude grid  
332 (the specific grid size is arbitrary). Down-sampling like this fixes the number of  
333 input features for each vortex and although it removes small-scale atmospheric  
334 phenomena from the sample, finer grids do not improve the accuracy of the ANN  
335 output at the cost of increased computation time for training and detection.

336 Each “vortex” in the training set is a grid of  $T$ ,  $U$ ,  $V$ ,  $\zeta_r$ , and latitude,  
337  $|\phi|$ , which are reshaped into a one-dimensional array to form the 180 nodes  
338 (“features”) of the input layer of the network ( $36$  grid points  $\times$   $5$  atmospheric  
339 parameters). The windows are also randomly “jittered” up to 20% about each  
340 vortex to create examples of off-centre detections that should allow the final  
341 algorithm to detect vortices even in cases of sub-optimal alignment. It also  
342 ensures that the number of examples of each vortex type is equal, such that  
343 each output class has equal weight during training (as an alternative method to  
344 asymmetric weighting coefficients, [James et al., 2020](#)).

345 Each network is trained with the range of architectures explored in Section  
346 [2.4.2](#), which produces a maximal training accuracy of 93%. Doubling the sam-  
347 pling density of the grid (thus squaring the number of features) improves this  
348 accuracy by 1%, implying that the accuracy is not overly sensitive to the level of  
349 detail provided by each sample. This accuracy is more likely to be a reflection  
350 of the small sample size of the training set (141 vortices). Such a high accuracy  
351 for such a small, and low-resolution dataset implies that the data is not being  
352 over-fitted and is promising for future implementations of this neural network

353 detection method (see Section 4).

354 Feature analysis techniques are used to determine the degree to which each  
355 feature (each pixel of atmospheric information) correlates with changes in each of  
356 the three output classes “not vortex”, “positive vortex”, and “negative vortex”  
357 (referring to the sign of relative vorticity,  $\zeta$ ). This is useful when there is no  
358 clear *a priori* knowledge of what variables to use. On such technique is the  
359 Analysis of Variance (ANOVA, James et al., 2020), and when implemented with  
360 only these five atmospheric parameters reveals temperature to have the greatest  
361 correlation with the output classification. Training the network using only the  
362 temperature field actually obtains a test accuracy of 83%, which is remarkable  
363 with so few vortices and such low spatial resolution. Broadly speaking, this  
364 could mean that the horizontal wind field is not necessary for neural network  
365 vortex detection. It may be possible to get a significant fraction of the efficacy  
366 of this method with temperature alone, which has implications for imaging data  
367 and spatially-resolved thermal retrievals (discussed in Section 4).

#### 368 2.4.2. Network architecture

369 In order to avoid over-fitting the data while retaining a good quality clas-  
370 sification, the network architecture of ANN approach is optimised as follows.  
371 The training data is used to obtain the matrix of weights and biases for a given  
372 architecture using the detection algorithm. In order to avoid under-fitting or  
373 over-fitting the data, we explore a space of possible architectures to obtain the  
374 optimal configuration. The architecture has one input layer with 180 nodes (the  
375 reshaped model fields), the intermediate hidden layers, and one output layer  
376 with 3 nodes (the three output classes) initialised with randomised weights and  
377 biases between the nodes. Each network architecture of 1, 2, and 3 hidden lay-  
378 ers with a range of nodes per hidden layer (logarithmically spaced between 2  
379 and 512) is trained fifty times to account for the statistical differences in each  
380 randomised matrix of weights and biases, and the *validation accuracy*,  $A$ , and  
381 *validation cost*,  $J$ , are calculated for each architecture. Validation accuracy is  
382 simply the ratio of correct predictions and total predictions (equal to one with

383 all correct predictions), and  $J$  is a measure of the difference between the real  
 384 and predicted value (equal to zero with a perfect prediction). It is evaluated  
 385 using 5-fold cross-validation (because of the statistically small size of the train-  
 386 ing set), which describes how skilled the network is at operating on an unseen  
 387 subset of the training data, as a way to evaluate the performance of a given  
 388 architecture (James et al., 2020). At this stage,  $J$  is a more useful metric for  
 389 constraining the optimal architecture than validation accuracy, since the latter  
 390 can change with the final implementation of the neural network and detection  
 391 algorithm.

392 The global minimum of  $J$  represents the optimal configuration of nodes and  
 393 layers, with node configurations below (fewer nodes) and above (more nodes)  
 394 the minimum corresponding to under-fitting the data (not well-trained on the  
 395 training data) and over-fitting the data (only trained on the training data, not  
 396 generalised for unseen data), respectively. Figure 3 shows that the optimal  
 397 configuration in each case is actually the one with the fewest hidden layers  
 398 (Figure 3a) and also the fewest overall nodes (i.e. the least complexity). The  
 399 final chosen network architecture is shown in Figure 4 and has an input layer  
 400 (180 nodes), one hidden layer (102 nodes), and the output layer (3 nodes).  
 401 This architecture was then trained once using all of the training samples, where  
 402 the labelled test set of samples was used to provide the final measure of ANN  
 403 accuracy equal to 93%.

#### 404 2.4.3. Detection algorithm

405 The final detection algorithm takes the binning scheme from Section 2.4.1,  
 406 the optimised weights and biases from Section 2.4.2, and applies them to the  
 407 entire unseen dataset of Saturn-DYNAMICO.

408 For this, the detection window is passed over each map sequentially in one-  
 409 degree increments for all latitude-longitude points  $(\phi, \lambda)$  across a small range  
 410 of aspect ratios and meridional diameters. From the manual study, it is clear  
 411 that most vortices exhibit an aspect ratio,  $AR = D_x/D_y$ , of 1.4, so by fixing the  
 412 aspect ratio and scanning a small range of meridional diameters ( $D_y = 4^\circ$  on

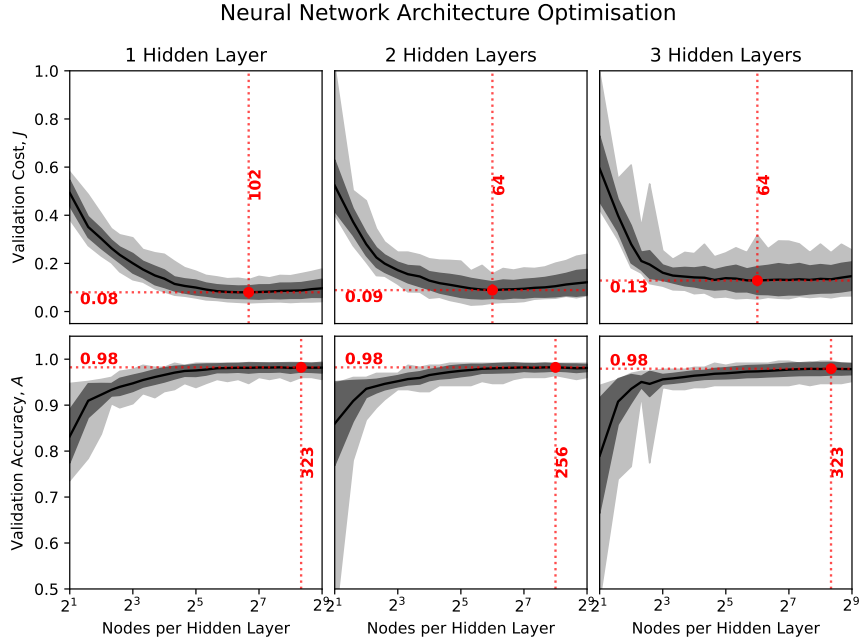


Figure 3: Validation cost (top) and validation accuracy (bottom) for architectures with 1, 2, and 3 hidden layers, with the optimal configuration highlighted in each. In each panel the solid curve is the mean value, the dark shaded region is one standard deviation about the mean, and the light shaded region is the range.

413 the model grid), it is possible to capture the vast majority ( $>95\%$ ) of vortices  
 414 while substantially reducing the computation time (in fact, size and aspect ratio  
 415 makes little difference to the ability of the ANN to detect a vortex). For each  
 416 instance, the contents of a window are evaluated by the network and the region  
 417 is given a probability according to how likely it is to not contain a vortex or to  
 418 contain a vortex of either sign. This process generates a two-dimensional prob-  
 419 ability matrix,  $p(\phi, \lambda)$ . The peaks in this two-dimensional probability matrix of  
 420 Class 1 or 2 correspond to cases with a high likelihood of a positive vortex identi-  
 421 fication. The configurations at these two-dimensional peaks can be found using  
 422 an assumed probability threshold, and the location and size of those vortices are  
 423 extracted to form the basis of the analysis of spatial, temporal, and dynamical

424 distributions (detailed in Section 3). The off-centre “partial” detection that jit-  
 425 tering offers, effectively increases the range of detection probabilities, widening  
 426 the probability peaks and reducing the sensitivity of the output to the final  
 427 selection threshold.

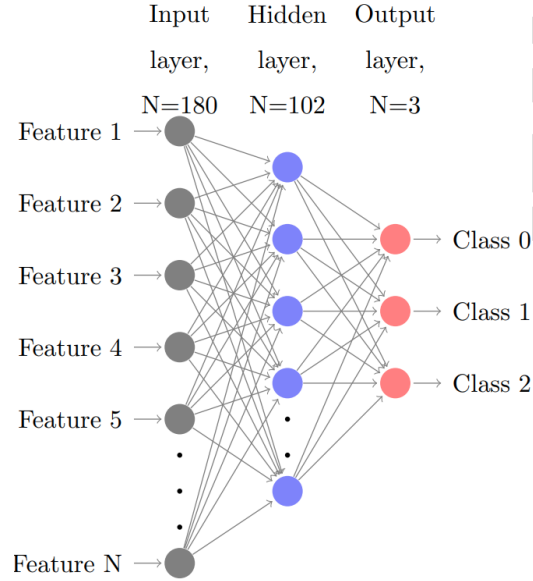


Figure 4: Schematic of the final neural network architecture. Each input node (grey) represents a feature, i.e. a grid point in the windowed model fields. These are passed to the hidden nodes (blue) then to the output nodes (red) which define the identity of the contents of the window. Bias nodes have been omitted for clarity and arrows represent the neural connections (weights not represented here).

#### 428 2.5. Dynamical detection - AMEDA

429 The dynamical approach utilises the Automated Eddy-Detection Algorithm  
 430 (AMEDA, [Le Vu et al., 2018](#)) that was developed for analysis of terrestrial  
 431 oceanic eddies. Since AMEDA processes directly the dynamical fields (rather  
 432 than pixel values) the vortex detection is different to the human eye and the  
 433 ANN, and occurs broadly in three stages. First, it searches locally by passing  
 434 a fixed window across the global map to find maxima in angular momentum of

435 either sign that coincide with negative maxima in the Okubo-Weiss parameter,  
436  $W$ . This corresponds to a location that has high angular momentum and is  
437 rotation-dominated, respectively, indicating an eddy or vortex. Then it identifies  
438 the largest closed streamline (contour of the streamfunction,  $\psi$ ) around that  
439 point which represents the eddy boundary. Finally, it evaluates the size of the  
440 feature with respect to a size-filtering parameter to which vortex detection is  
441 highly sensitive and which must be well-justified.

442 Parametric testing was carried out on all input parameters and the output  
443 was found to be slightly sensitive to two scanning parameters but almost entirely  
444 sensitive to the size-filtering parameter. The two scanning parameters specified  
445 the number of streamlines that are scanned about the angular momentum  
446 maximum and the number of points required along a  $\psi$ -contour to define a  
447 streamline. In both cases we found that a higher or lower detection rate simply  
448 implied that it was simply more or less difficult to identify streamlines in the  
449 vicinity of the angular momentum maximum, rather than there actually being  
450 more or fewer vortices found. So it is sufficient to fix these to the values used  
451 in [Le Vu et al. \(2018\)](#).

452 This size-filtering parameter AMEDA uses to isolate large-scale vortices from  
453 the small-scale eddies is a tunable spatial scale governed by the Rossby deforma-  
454 tion radius, which is the typical scale of large-scale waves arising from baroclinic  
455 instabilities and is the characteristic spatial scale at which an eddy may develop  
456 into a coherent vortical structure. This scale is not a clear transition, but more  
457 a consideration for the approximate scales at which vortices are likely to form.  
458 The filtering parameter is defined as the ratio of feature size in pixels to the  
459 Rossby deformation radius. This is a reasonable, albeit ambiguous, condition for  
460 the rejection or retention of vorticity features. The Rossby scale is particularly  
461 difficult to estimate in the atmospheres of gas giants. However, the horizontal  
462 resolution of DYNAMICO enables the resolution of eddy-driven instabilities in  
463 Saturn's atmosphere, by resolving the Rossby deformation radius on-line, so  
464 it is generally not calculated during modelling. Thus, we estimate it through  
465 a sensitivity test with AMEDA (reinforcing the observer-oriented focus of this

466 work).

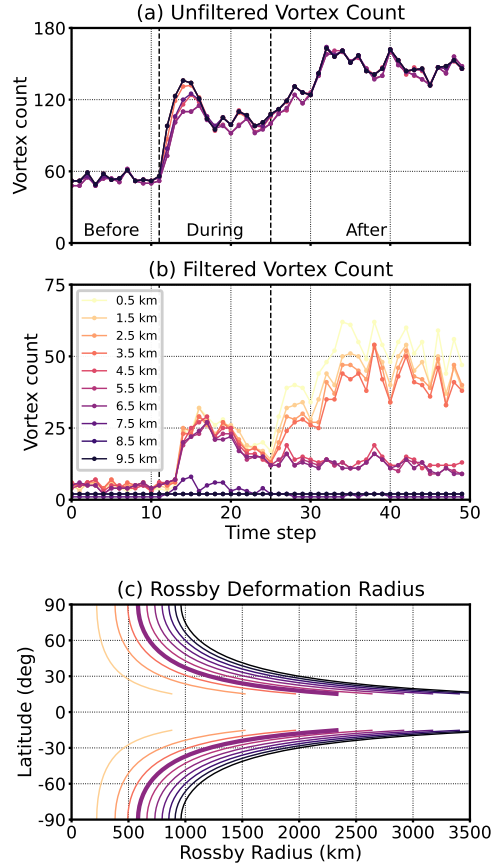


Figure 5: AMEDA sensitivity analysis of the event in Figure 1 showing the stages over 1000 model days before, during, and after the eddy-burst. (a) Overall count of detected vortices across range of Rossby layer thicknesses with no spatial filtering, (b) the same count with the spatial filtering applied to the eddy-burst, and (c) the corresponding meridional profiles of Rossby deformation radius. All panels use the same legend. Black dashed vertical lines in (a) and (b) represent the different stages of the event, corresponding to Figure 1. Thick line in (c) is the 6.5-km solution chosen for this study.

467 As a null hypothesis, we estimate the *barotropic* Rossby deformation radius,  
 468  $L_{bt} = \frac{\sqrt{gD}}{f}$  (Holton, 2004), where  $g$  is the gravitational acceleration,  $f$  is the  
 469 Coriolis parameter, and  $D$  is the thickness of the layer, equal to the distance

470 between the model base and “cloud-top” reference level ( $\sim 82$  km). This gives  
 471 an upper estimate of  $L_{bt} \sim 10000$  km in the middle latitudes. This is an order of  
 472 magnitude larger than the first *baroclinic* Rossby deformation radius,  $L_{bc} = \frac{NH}{\pi f}$   
 473 (Holton, 2004), inferred from the Brunt-Väisälä frequency,  $N$ , of Spiga et al.  
 474 (2020) at this reference level ( $L_{bc} = 1333$  km). Thus, the atmosphere between  
 475 the model base and the cloud top cannot be represented as a single barotropic  
 476 layer.

477 As a lower estimate, the *barotropic* Rossby deformation radius calculated for  
 478 an atmospheric layer with the thickness of one model level is  $L_{bt} = 935$  km, quite  
 479 similar to the *baroclinic* value inferred from Spiga et al. (2020). Therefore, if we  
 480 treat this atmospheric layer as being under *baroclinic* conditions for the purpose  
 481 of obtaining a meridional profile of Rossby deformation radius for testing, we  
 482 may model it simply using the *barotropic* equation for a suitably shallow layer.  
 483 By testing a range of these “equivalent layer” thicknesses we obtain a range of  
 484 Rossby deformation radius profiles and vary the size of the vorticity features  
 485 that pass through the filter and can assess how sensitive the AMEDA outputs  
 486 are to our Rossby scale assumptions.

487 Meridional profiles of Rossby deformation radius associated with barotropic  
 488 layers of varying thickness are used to determine the magnitude of the filtering  
 489 parameter as a function of latitude (Figure 5). If the feature’s size is equal to  
 490 or larger than this scale it passes through the filter. Before applying the spa-  
 491 tial filter, AMEDA greatly over-samples the vorticity field, selecting as many  
 492 distinct maxima of angular momentum as possible, regardless of size. When  
 493 applying the spatial filtering, the thickest equivalent layers of 7.5-9.5 km (cor-  
 494 responding to the largest Rossby scales) are unable to retain even the largest  
 495 vortices throughout the event. During the event from time step 11-25, shallower  
 496 equivalent layers of 0.5-6.5 km (corresponding to smaller Rossby scales) detect  
 497 all vorticity features whether they are eddies or vortices. After the event beyond  
 498 time step 25, equivalent layers in the range of 4.5-6.5 km thick (corresponding  
 499 to Rossby scales of 700-1000 km in the middle latitudes) filter out most of the  
 500 small-scale eddies and leave most of the large-scale vortices.



501 This filtering is imperfect as it is possible to lose the smallest of the coherent  
502 vortices. However, in the context of the manual and ANN methods (see Section  
503 3) these smallest vortices do not comprise a significant portion of the vortices  
504 found in the model. Figure 5 shows that DYNAMICO does in fact capture  
505 the clear selection of spatial scales for cyclogenesis that is expected from first  
506 principles.

507 Following the filtering step, AMEDA returns the location and spatial bounds  
508 of each vortex, producing the spatial distributions discussed in Section 3. Addi-  
509 tionally, AMEDA automatically calculates the mean radius of each vortex as a  
510 circle with the same area as one enclosed by the closed streamline. From this, a  
511 mean velocity profile is derived from the circulation along the closed streamline  
512 (Le Vu et al., 2018). The peak of the mean velocity profile is reasonably assumed  
513 here to be the vortex edge. The assumption of circularity is used here only for  
514 this calculation as the actual shape is retained for the purposes of studying the  
515 spatial structures. This step is intended as a way to explore the internal dy-  
516 namics of each vortex and the results are shown in Figure 10 and discussed in  
517 Section 3.

### 518 3. Results

519 The distributions of location, size, shape, zonal winds, and vortex intensity  
520 generated by these three methods are compared below, with the total vortex  
521 count, annual count rate derived from the seasonal average of counts, and mean  
522 aspect ratio summarised in Table 1. Additionally, the AMEDA results are  
523 used to explore vortex dynamics along vortex boundaries with the edge velocity  
524 profiles and interiors with an inter-comparison of the three Okubo-Weiss pa-  
525 rameters. Finally, a short discussion of the planetary Burger number (defined  
526 in Section 3.5) is proposed, discussing the great diversity of polar regimes and  
527 configurations of polar vortices in the giant planets, and implications for future  
528 study.

529 *3.1. Spatial and temporal distribution*

530 All large-scale vortices in the Saturn-DYNAMICO model are clustered in  
 531 latitude and are present in regions of cyclonic and anticyclonic shear in the  
 532 zonal wind (as in Vasavada et al., 2006). They are found exclusively beyond  $60^\circ$   
 533 latitude in each hemisphere at the highest-latitude westward jets, with slightly  
 534 more in the south (as in Trammell et al., 2014). This strong correlation with  
 535 the jet locations follows the poleward migration of the jet structure that was  
 536 reported in Spiga et al. (2020), further confirmation that these vortices are re-  
 537 producing expected behaviours. Unlike the observed vortices of Trammell et al.  
 538 (2014, 2016), the model produces no large-scale vortices at latitudes lower than  
 539 this. This is likely because the criterion for barotropic instability, a necessary  
 540 but insufficient condition for generation of these vortices (Spiga et al., 2020),

Method	Sense ( $\zeta/f$ )	Total Vortex Count			Count Rate (year <sup>-1</sup> )			Mean AR
		Global	NH	SH	Global	NH	SH	
Manual	Both	141	63	78	20.14	9.00	11.14	–
	+ve	82	33	49	11.71	4.71	7.00	1.44
	-ve	59	30	29	8.43	4.29	4.14	1.13
ANN	Both	96404	51844	44560	48.59	26.61	21.97	–
	+ve	58729	27811	30918	28.81	14.48	14.34	1.54
	-ve	37675	24033	13642	19.77	12.13	7.64	1.38
AMEDA	Both	552	273	279	17.73	9.54	8.19	–
	+ve	321	131	190	10.19	4.93	5.26	1.47
	-ve	231	142	89	7.54	4.61	2.93	0.98

Table 1: Summary of primary statistics of vortices in the GCM for each method. Columns show the vortex sense as determined by the sign of the planetary-normalised relative vorticity,  $\zeta/f$  (positive for cyclones and negative for anticyclones), the total raw vortex counts, and the annual count rate calculated from the seasonal average of raw vortex counts over 7 model years. All counts are separated by vortex sense and hemisphere (NH and SH for north and south hemispheres, respectively). Aspect ratios (AR) are expressed as a global average, separated only by vortex sense.

541 does not change sign in the domain of the low and mid latitudes. Even if they  
542 were produced, the spatial resolution of the model (one half-degree grid cell  
543 at the equator spans  $\sim 500$  km), they would be difficult to detect with these  
544 methods since the median size vortex would be 2-4 grid points (1000-2000 km  
545 across), as discussed in Section 3.4). In contrast, low- and mid-latitude vortices  
546 towards the larger end of the size distribution ( $>10$  grid points) would be easier  
547 to detect.

548 The manual method has lower temporal sampling than the automated meth-  
549 ods so we express the vortex counts as a seasonal average as also a way to  
550 partly control for repeated sampling of long-lived vortices that span multiple  
551 model time steps in a given season. This is a moderate sampling bias as we do  
552 not sample unique vortices, but it is sufficient to build up a a statistical view  
553 of the instantaneous structure of vortices. The manual method is treated as  
554 a seasonal average by experimental design (see Section 2.3), so the ANN and  
555 AMEDA methods are averaged onto the same temporal grid by averaging the  
556 vortex counts over multiple model time steps per season. The raw vortex counts  
557 and annual count rates (derived from the seasonal averages) are found in Table  
558 1. The automated methods have a common temporal sampling, so difference in  
559 counts between the two methods directly reflects differences between the neural  
560 network and dynamical approaches.

561 Comparing the seasonally-averaged vortex counts, the manual method found  
562 141 vortices in total, while the ANN and AMEDA methods found 340 and 120,  
563 respectively. Figure 6 shows the vortex counts and locations as a function of  
564 time for each of the three methods. While the methods return similar seasonally-  
565 averaged vortex count over time, there are some differences that reflect the  
566 fundamental differences between them. This is seen clearly in model year 14, in  
567 which there was a particularly large eddy-burst event that left the south polar  
568 region very disrupted with a disorganised structure of eddies that progressively  
569 merged into fewer and larger vortices. During the disrupted state, the human eye  
570 can reasonably distinguish near-circular vortices from the smaller-scale eddies.  
571 However, AMEDA relies on the clear detection of closed streamlines and has

572 difficulty in resolving anything other than the most dominant polar cyclone and  
 573 anticyclone for most of the outburst. Another notable difference is the 3-10  
 574 times higher detection rate of the ANN method in model year 8.

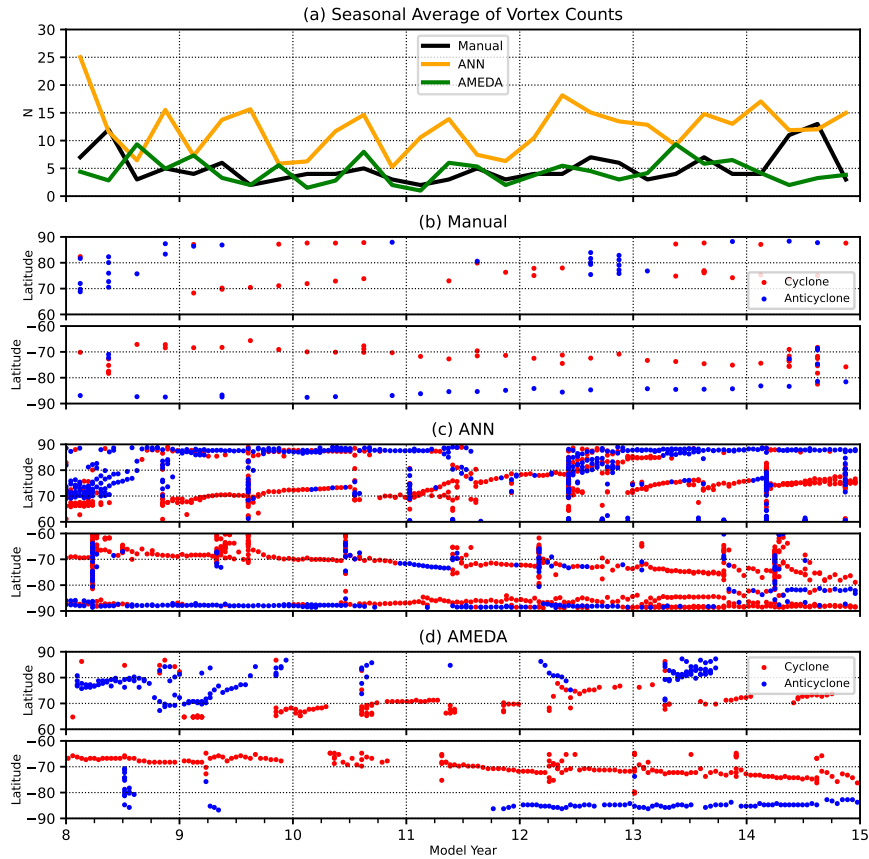


Figure 6: Time series of (a) seasonally-averaged vortex counts and (b-d) spatial distribution of vortices separated by vortex sense for the manual, ANN, and AMEDA methods, respectively.

575 With the benefit of the long time series of simulated model years, there is a  
 576 tentative seasonal variability in vortex count but not in spatial distribution (the  
 577 latter is in agreement with observations by [Trammell et al., 2014, 2016](#)). We also  
 578 see a lack of variability associated with the long-term changes in atmospheric

579 temperature, supporting the conclusion of Trammell et al. (2016) that large-  
 580 scale thermal structure and circulation are not directly affected by the temporal  
 581 variation of vortices. However, there is an inter-annual shift from more northern  
 582 vortices earlier in the model to more southern vortices later, but this is likely  
 583 incidental, being a function more of the spontaneous eddy-burst events than  
 584 any long-term changes in atmospheric structure.

### 585 3.2. Size and shape distribution

586 The vortices generated in Saturn-DYNAMICO are generally much larger  
 587 than observed vortices. This is more likely due to a greater latitudinal spacing  
 588 between the modelled zonal jets than the characteristic jets of the planet Saturn.  
 589 This renders absolute estimates of vortex size useful when comparing model  
 590 parameterisations (and thus modelled jet structures), but not particularly useful  
 591 in direct comparison to observations. However, the overall shape of the size  
 592 distribution can provide relative insights to those of the planet Saturn.

593 With all methods we see an order-of-magnitude correlation between over-  
 594 all size and Rossby deformation radius, which is expected by Trammell et al.  
 595 (2016) and reinforced by the efficient eddy filtering in AMEDA. Figure 7 shows  
 596 the distribution of mean vortex radius,  $\bar{R} = \frac{1}{2}(D_x + D_y)$ , in units of Rossby  
 597 deformation radius. With the manual and AMEDA methods we do not find any  
 598 vortices below  $\sim 1000$  km (or  $1 L_{bt}$ , the systematic assumption made to reject  
 599 eddies below this characteristic spatial scale). However, the manual method  
 600 do not have this assumption, yet reproduce the same minimum vortex size as  
 601 AMEDA and observations (Trammell et al., 2014, 2016), confirming the utility  
 602 of the filtering assumptions for AMEDA. Note that ANN-detected vortices are  
 603 often smaller than this threshold, suggesting an erroneous detection of features  
 604 smaller than the Rossby length scale.

605 Figure 8 shows that in most cases the vortices peak towards smaller values  
 606 at  $\sim 5000$ - $7000$  km, and have a long tail extending to  $\sim 15000$ - $18000$  km in very  
 607 low concentrations ( $\leq 1\%$  of vortices). In the AMEDA case there is a sharp  
 608 drop-off after  $7000$  km in both the zonal and meridional directions. Since eddy

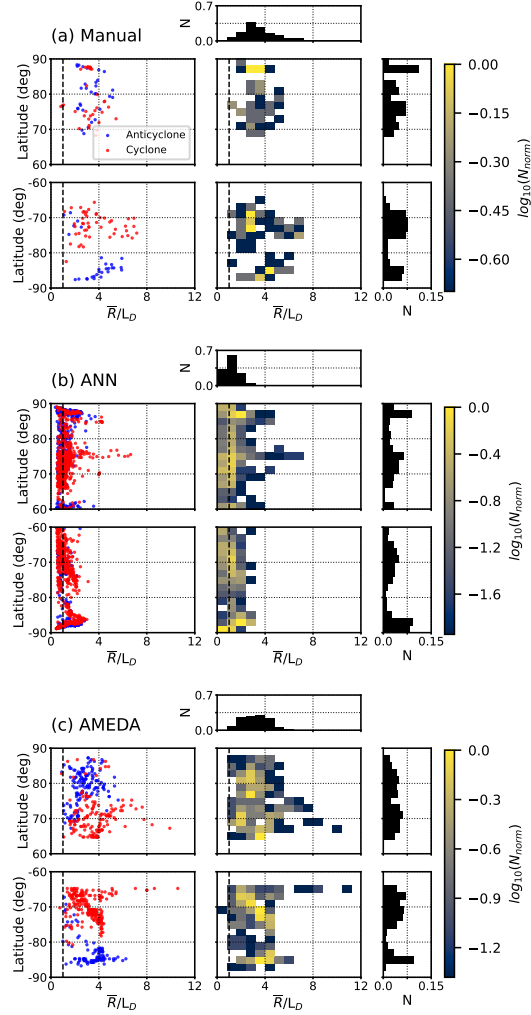


Figure 7: Size distribution of vortices in the GCM for (a) manual, (b) ANN, and (c) AMEDA methods. (Left) Rossby-normalised average size as a function of latitude as a scatter separated by vortex sense, and (right) 2D joint probability density histogram of number density,  $N$ , with 1D histogram components bounding the relevant axis. 2D histogram data is normalised to the data range, such that  $N_{\text{norm}} = \frac{N - N_{\text{min}}}{N_{\text{max}} - N_{\text{min}}}$ , and colour values are distributed logarithmically as  $\log_{10}(N_{\text{norm}})$ . Dashed line corresponds to  $\bar{R}/L_D = 1$ .

609 filtering is performed with respect to Rossby deformation radius, it is not clear  
 610 there should be such a strong selection of absolute spatial scale in comparison to

611 other methods. [Vasavada et al. \(2006\)](#) observe a wide range of sizes in regions of  
612 cyclonic shear, but despite a few exceptionally-large cyclones, wide distributions  
613 are seen in all regions independent of shear sense. The maximum size of modelled  
614 vortices is greater than observations by a factor of two (Voyager/ISS, [Rogers,](#)  
615 [1995](#)) and three (Cassini/ISS, [Trammell et al., 2014, 2016](#)). So while the model  
616 spatial resolution at lower latitudes might preclude detection of the smallest  
617 vortices, vortices of this larger size were simply not observed in the atmosphere  
618 of Saturn, with the exclusive exception of the polar vortex as measured by the  
619 Pic du Midi (7000-11000 km, [Sánchez-Lavega et al., 1993, 1997](#)).

620 Figure 8 shows the distributions of zonal and meridional diameters, organised  
621 by aspect ratio and shape. Most vortices are circular or zonally-oblate across  
622 all methods (not surprising in the manual and ANN case since it is an explicit  
623 assumption), implying a greater propensity for vortex growth in the zonal direc-  
624 tion than the meridional direction. The manual approach appears to show no  
625 clear differences in shape between cyclones and anticyclones with a least-squares  
626 fit through the entire distribution (in agreement with [Trammell et al., 2016](#), but  
627 with more circular vortices overall). The expectation from observations should  
628 be more like the AMEDA result with anticyclones being more circular and with  
629 a narrower range of aspect ratios, and cyclones having a much wider range of  
630 aspect ratios and sometimes being very zonally oblate (e.g. anticyclonic white  
631 ovals compared to cyclonic brown barges, [Rogers, 1995](#); [Morales-Juberías et al.,](#)  
632 [2002](#); [Legarreta and Sánchez-Lavega, 2005](#); [Rogers, 2007](#); [Rogers et al., 2010](#);  
633 [Orton et al., 2015](#); [Fletcher et al., 2017a](#)). Indeed this is exactly the case for  
634 the most common value of aspect ratio for all methods, seen in Table 1.

### 635 3.3. Vortex winds

636 Barotropic instability seems to be a necessary but not sufficient condition  
637 for cyclogenesis in DYNAMICO. This is because cyclogenesis occurs exclusively  
638 at the highest-latitude westward jets, where the Rayleigh-Kuo criterion for  
639 barotropic instability is frequently violated, and not seen at the barotropically-  
640 stable low and middle latitudes where it is not violated ([Spiga et al., 2020](#)).

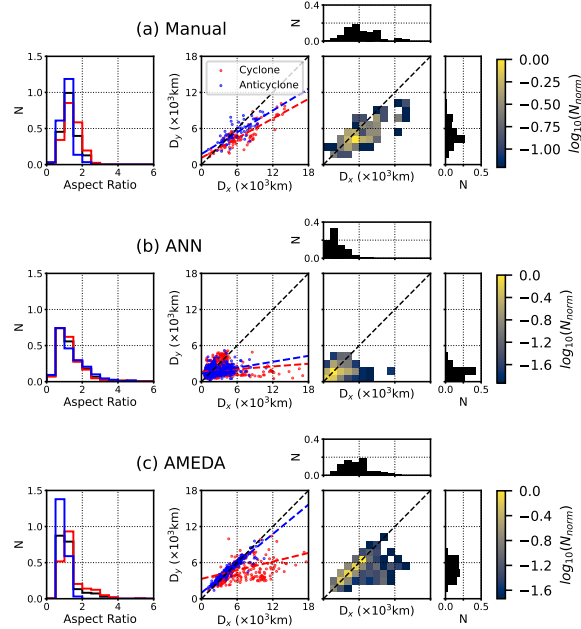


Figure 8: Shape distribution of vortices in the GCM for (a) manual, (b) ANN, and (c) AMEDA methods. (Left) 1D histogram of aspect ratio and (centre) scatter of zonal and meridional diameters separated by vortex sense, and (right) 2D joint probability density histogram of number density (colour scale based on that of Figure 7).

641 If we treat each vortex centre as instantaneously stationary with respect to  
 642 the mean flow, we can get an estimate of the zonal wind at the vortex location  
 643 which we can use as a proxy for drift rate. Figure 9 shows that most vortices  
 644 form very close to the average zonal-mean zonal-wind profile for the entire DY-  
 645 NAMICO simulation with a small fraction being associated with high rates of  
 646 prograde and retrograde drift about the mean flow. Cyclones and anticyclones  
 647 generally exhibit similar ranges of drift velocities throughout the model, but the  
 648 largest drift rates are exhibited by the anticyclones. Future investigations will  
 649 use the extended functionality of AMEDA to track the short-term evolution of  
 650 vortices as described in [Le Vu et al. \(2018\)](#), including direct measurements of  
 651 the drift rate and vortex interactions (merging/splitting events).

652 Vortex generation and stability can be understood through the mechanism



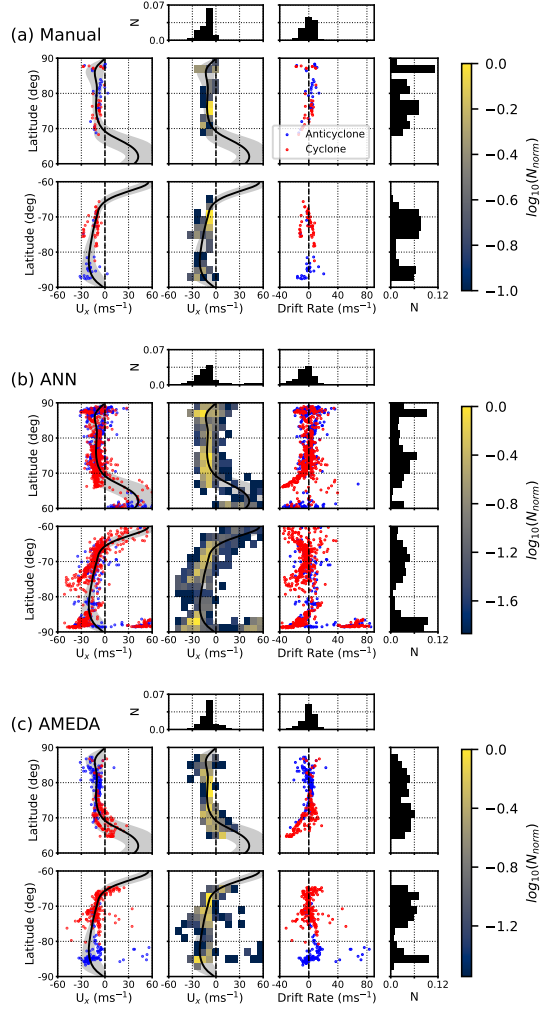


Figure 9: Local zonal wind and drift rates of vortices in the GCM for (a) manual, (b) ANN, and (c) AMEDA methods. (Left) scatter of the zonal wind velocity at vortex centre, (centre) 2D joint probability density histogram of number density (colour scale based on that of Figure 7), and (right) scatter of the relative velocity of the vortices with respect to the mean flow. Scatters are separated by vortex sense.

653 of cyclogeostrophic adjustment during frontogenesis according to [Shakespeare](#)  
 654 (2016). In the idealised case, a straight, uniform pressure gradient field can  
 655 establish a straight front, a boundary that separates air masses with differing

656 characteristics (e.g. density, temperature, pressure, or wind speed). The front  
 657 is increasingly subject to Coriolis acceleration as it increases in latitude, causing  
 658 frontal curvature through geostrophic adjustment. This curvature generates a  
 659 centripetal acceleration which acts to further increase curvature in proportion to  
 660 the ratio of centripetal and Coriolis acceleration, i.e., through *cyclogeostrophic*  
 661 adjustment. Frontal velocities become so high along this increasingly curved  
 662 front that eddy growth is strongly limited and a distinct vortex may be estab-  
 663 lished.

664 Stable fronts like those of the steady-state thermal field in the Saturn-  
 665 DYNAMICO GCM can suddenly be subject to rapid forcing from the kind  
 666 of quasi-periodic large-scale eddy-burst events that are ubiquitous in the model  
 667 (Spiga et al., 2020). This could reasonably result in the latitudinal deviation  
 668 required to cause geostrophic adjustment. Then surrounding conditions, those  
 669 which vary on the scale of several model grid points (a few degrees in latitude  
 670 or a few thousand kilometres, comparable to the upper range of the terrestrial  
 671 mesoscale, 200-1000 km) need only be sufficient to encourage further curva-  
 672 ture through centripetal acceleration and subsequent vortex stabilisation. So it  
 673 should be the surrounding conditions which determine the eventual structure  
 674 and dynamics of the GCM vortices.

675 Figure 10a shows that all vortices found in the model are cyclostrophic yet  
 676 it is not clear how important geostrophic curvature is to the vortex dynamics in  
 677 DYNAMICO. According to Shakespeare (2016), if at least one of the following  
 678 conditions is true, the curved fronts (eddies or vortices) can be considered to  
 679 be in *cyclogeostrophic* balance: (i) frontal velocity (analogous to vortex edge  
 680 velocity,  $V_{max}$ ) is high, (ii) radius of curvature (radius at maximum velocity,  
 681  $R_{max}$ ) is small, or (iii) latitude,  $\phi$  (or Coriolis parameter,  $f$ ), is small. From  
 682 Figure 10b it can be reasonably concluded that the former two conditions are  
 683 satisfied, even though the latter is clearly not, since all vortices are found beyond  
 684  $60^\circ$  of latitude (indeed, on a quickly-rotating body like Saturn, it is difficult to  
 685 have a small Coriolis parameter unless very close to the equator). Therefore, we  
 686 may represent the cyclogeostrophic curvature as the ratio of the centripetal and

687 Coriolis accelerations, the so-called *cyclogeostrophic* Rossby number,  $C = v/fr$ ,  
 688 (Mkhinini et al.; Shakespeare, 2016). Cyclogeostrophic curvature is important  
 689 to the dynamics if  $C$  is non-negligible.

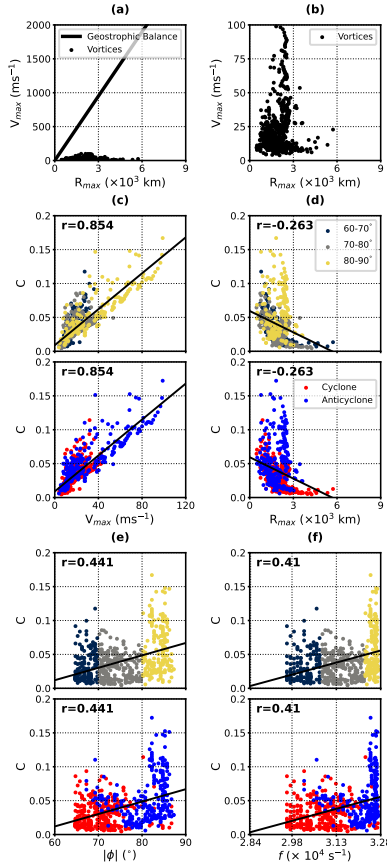


Figure 10: Vortex dynamics in the polar regions as measured by AMEDA. Vortex edge velocity as a function of vortex radius for all detected vortices (black points), (a) with and (b) without the geostrophic balance condition assuming  $Ro = 1$  (black line). Cyclogeostrophic Rossby number,  $C$ , as a function of (c)  $V_{max}$ , (d)  $R_{max}$ , (e)  $|\phi|$ , and (f)  $f$ , separated by latitude domain, and with linear fit and Pearson correlation coefficient.

690 Figure 10(c-f) shows that the cyclogeostrophic Rossby number,  $C$ , is indeed  
 691 non-negligible ( $< 0.18$ ) for the vortices, thus cyclogeostrophic curvature is mod-  
 692 ifying the speeds by up to 18% with respect to the geostrophic prediction. This

693 is below the range found for jovian vortices measured by Voyager/ISS and the  
 694 Galileo instrument (Legarreta and Sánchez-Lavega, 2005). However, it is simi-  
 695 lar to low- and mid-latitude terrestrial oceanic eddies, which have observed  $C$   
 696 values of 0.1-0.3 for the Gulf Stream meanders (Liu and Rossby, 1993), and  
 697 0.25 in the equatorial Pacific (Flament et al., 1996; Holmes et al., 2014) and  
 698 the Kuroshio Extension in the northwestern Pacific (Niiler et al., 2003). Here  
 699 we also see that  $C$  is moderately positively correlated with  $V_{max}$  ( $r = 0.854$ )  
 700 and minimally with  $\phi$  and  $f$  ( $r = 0.441$  and  $0.410$ , respectively), and negligibly  
 701 negatively correlated with  $R_{max}$  ( $r = -0.263$ ). Conversely,  $C$  values close to  
 702 zero indicate that curvature is not important and the front is close to geostro-  
 703 phy, which is roughly true for the slowest, lowest-latitude, and largest vortices  
 704 observed here.

#### 705 3.4. Vortex dynamics

706 Theory predicts that frontal curvature about a warm-core vortex (terrestrial  
 707 anticyclone) should act to increase velocities, and curvature about a cold-core  
 708 vortex (terrestrial cyclone) should decrease velocities (Shakespeare, 2016). This  
 709 is reversed for vortices in the upper troposphere of gas giants due to the lack  
 710 of a lower boundary layer (e.g. like the terrestrial surface) inverting the energy  
 711 dissipation scheme (Ingersoll et al., 2021). Furthermore, higher frontal velocities  
 712 in opposite-sign vortices (vortex sense has opposite sign to background shear)  
 713 should act to make them less stable and more prone to dissipation or instability  
 714 during adjustment (Hoskins and Bretherton, 1972; Rudnick, 2001; Scherbina  
 715 et al., 2013), reducing the number of opposite-sign vortices produced in the  
 716 model.

717 Figure 11 shows the distribution of planetary-normalised relative vorticity,  
 718  $\zeta_r/f$ , the ratio of the relative and planetary terms and a measure which is always  
 719 positive for cyclones and negative for anticyclones.

720 Since we do not observe warm-core cyclones with high frontal velocities, it  
 721 might be that they are forming in the Saturn-DYNAMICO model but dissipat-  
 722 ing more quickly than their anticyclonic counterparts. If cyclones are generally

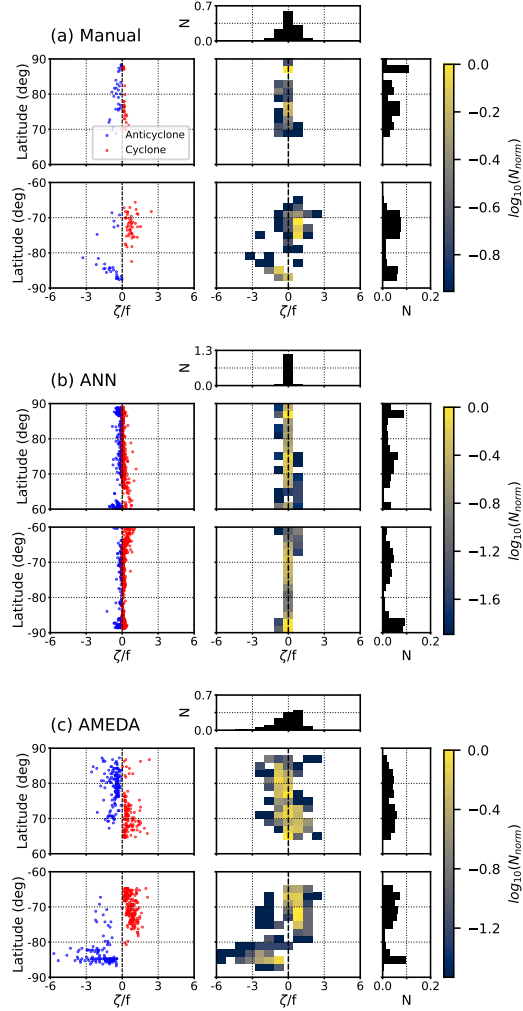


Figure 11: Distribution of vortex intensities in the GCM for (a) manual, (b) ANN, and (c) AMEDA methods. (Left) scatter of the planetary-normalised relative vorticity at vortex centre separated by vortex sense, (right) 2D joint probability density histogram of number density (colour scale based on that of Figure 7).

723 more likely than anticyclones to be dissipated when they are of opposite sign to  
 724 the shear region, then cyclones should be generally less common in anticyclonic  
 725 shear regions than anticyclones are in cyclonic shear regions. Indeed, unlike the

726 observations of Vasavada et al. (2006) but similar the theoretical predictions of  
 727 (Scherbina et al., 2013) (allowing for the inversion of the momentum dissipation  
 728 scheme above), the modelled vortices are actually more common in cyclonic  
 729 shear regions, despite the dominant selection mechanism of anticyclones. This  
 730 asymmetry is reflected in Figure 11 and is more pronounced in the north. The  
 731 origin of this hemispheric asymmetry is not clear, but is likely simply a result  
 732 of the sporadic eddy-bursts.

733 In the model, the dearth of anticyclones relative to cyclones ( $n_a/n_c \approx 0.7$ )  
 734 seen in Table 1 and Figures 11, 12, and 13 is in stark contrast to the putative  
 735 nature of the upper tropospheres of the gas giants which are expected to have  
 736 an anticyclonic bias. However, in the Saturn-DYNAMICO model the cyclonic  
 737 shear regions are simply much larger than anticyclonic shear regions, so even  
 738 with a symmetric dissipation, same-sign selection implies that we might still  
 739 expect more cyclones overall. Essentially, if the zonal wind profile looked more  
 740 like Saturn the vortex distributions likely would as well.

741 We note here that the planetary-normalised vorticity of the ANN method is  
 742 an order-of-magnitude lower than the others. The dominance of low vorticities  
 743 can be explained by the prevalence of sub-Rossby scale features, but it is unclear  
 744 why we are missing the largest vorticities, especially since all methods produce  
 745 similar size distributions.

746 Since the AMEDA method reliably detects a large number of vortices, with  
 747 associated quantitative diagnostics, we use that dataset to further explore the  
 748 three Okubo-Weiss parameters. These three parameters provide a useful diag-  
 749 nostic for vortex dynamics that will be used as a metric for future comparative  
 750 studies (see Section 4). They are calculated for all detected vortices and com-  
 751 pared to the planetary state overall (all polar grid cells within  $\pm 60$ - $90^\circ$  latitude).  
 752 The probability density histograms are displayed in Figure 12 and combined in  
 753 Figure 13 to give a more general view of rotation and deformation characteris-  
 754 tics, as a comparative metric to the terrestrial oceanic studies that inspired this  
 755 aspect of the analysis (Rudnick, 2001; Scherbina et al., 2013).

756 The vorticity distributions in Figure 12a and 12d are that of 11c and show

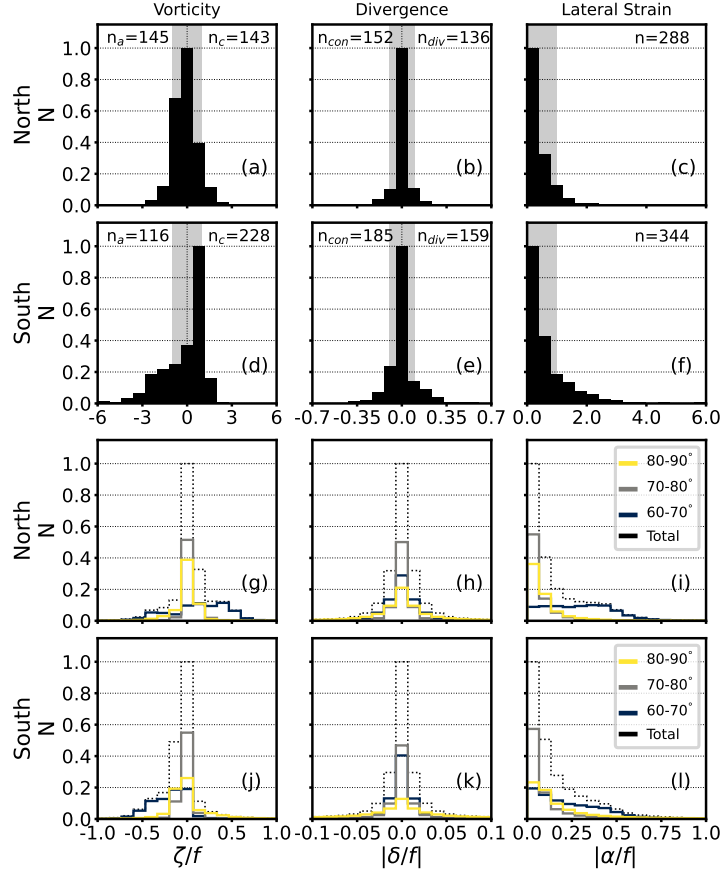


Figure 12: Distribution of Okubo-Weiss diagnostics. Histograms of planetary-normalised vorticity, divergence, and lateral strain separated by hemisphere and normalised to maximum counts for all vortices (a-f) and all model grid cells (g-i). Coloured histograms (g-i) show the parameters in the same latitude ranges as Figure 10.

757 the same northern symmetry of intensity and vortex sense and the southern  
 758 asymmetry with a higher number of cyclones and stronger anticyclones. This  
 759 means that weak vortices are more likely to be cyclonic, moderately-strong  
 760 vortices are more likely to be anticyclonic, and the strongest vortices are always  
 761 anticyclonic. A similar hemispheric trend is seen in the divergence distribution  
 762 with a slightly more pronounced northern asymmetry and much smaller overall

763 magnitudes compared to vorticity and strain. The distribution of lateral strain  
 764 rates adds to this picture in the same way, showing that vortices in the south  
 765 polar region are generally a lot more dynamically diverse than those in the  
 766 north.

767 This kind of hemispheric asymmetry is difficult to observe on gas giants  
 768 without highly-resolved imaging and cloud-tracked wind measurements of both  
 769 polar regions. However, Siegelman et al. (2022a) characterise the north polar  
 770 region of Jupiter with Juno/JIRAM images and show that vorticities within  
 771 the circumpolar vortices can reach magnitudes on the scale of the planetary  
 772 vorticity ( $\zeta/f \sim 1$ ). They observed much smaller relative magnitudes of hori-  
 773 zontal divergence,  $\delta$  (Equation 2), similar to DYNAMICO, implying that these  
 774 vortices are dominated by two-dimensional turbulence at these spatial scales.  
 775 Future studies that explore the south polar region in the context of these JI-  
 776 RAM images and this dynamical study will add much-needed context to the  
 777 study of vortex dynamics.

778 Joint probability density histograms in Figure 13 show the relative shapes  
 779 of these distributions. Considering the lateral strain rate,  $\alpha$  (Equation 3), with  
 780 respect to the vorticity gives an indication of whether the vortex is in an eddy  
 781 regime ( $\alpha < |\zeta|$ ), a shear regime ( $\alpha = |\zeta|$ ), or a strain regime ( $\alpha > |\zeta|$ ). For ex-  
 782 ample, the peaks of the zonal jets are a purely shear regime and are seen in the  
 783 clustering of values around the diagonal lines in Figure 13e. Figure 13c shows  
 784 that smaller, weaker vortices lie close to but below the shear regime, reflecting  
 785 their short-lived and transient nature, forming and dissipating quickly follow-  
 786 ing a large eddy-burst event. However, some small vortices are also strongly  
 787 rotation-dominated despite their weak vorticity, which is more true for anticy-  
 788 clones than cyclones. Anything in between these lines in the eddy-shear regime  
 789 corresponds to a cyclogeostrophic front with varying magnitudes of rotation.

790 Finally, we gather together all of the statistical parameters from this work  
 791 to summarise their relative differences between all cyclones and anticyclones de-  
 792 tected in the Saturn-DYNAMICO simulation. All distributions are normalised  
 793 so that they vary between 0 and 1. This removes absolute differences between



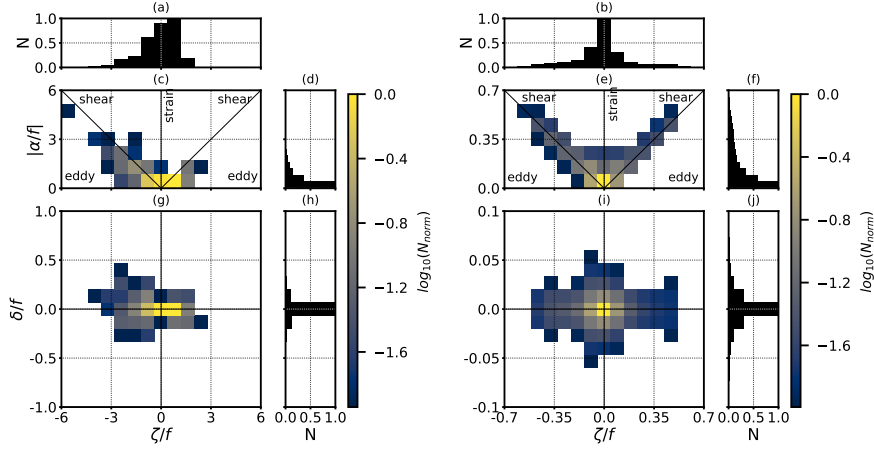


Figure 13: Distribution of Okubo-Weiss diagnostics. 2D joint probability density histogram of number density (colour scale based on that of Figure 7) constructed from the global distributions of rotation and deformation terms in Figure 12. The left group shows values for the vortices (a, c, d, g, h) and the right group shows values for all grid cells in the polar regions (b, e, f, i, j). The black diagonal lines correspond to one-dimensional shear flow and the horizontal line  $|\alpha/f| = 0$  corresponds to solid-body rotation.

794 the parameters and instead emphasises the relative distributions for cyclones  
 795 and anticyclones. The multivariate distributions in Figure 14 reinforce the con-  
 796 clusion that cyclones are more spatially diverse (they exhibit a greater range of  
 797 sizes and shapes) and anticyclones are more dynamically diverse (they exhibit a  
 798 greater range of edge velocities, drift rates, Okubo-Weiss parameters), and they  
 799 provide a useful “fingerprint” for future comparative studies of vortex statistics.

### 800 3.5. Polar regimes

801 The polar regions of the Saturn-DYNAMICO GCM exhibit a great diversity  
 802 of circumpolar jet and vortex configurations, at different times resembling all  
 803 of the giant planets in the Solar System. Brueshaber et al. (2019) discuss the  
 804 planetary Burger number,  $Bu = (L_D/a)^2$  (Read, 2011), as it relates the Rossby  
 805 deformation radius and corrected polar radius,  $a$ , to the structure of polar vor-  
 806 tices as observed on Jupiter, Saturn, Uranus, and Neptune. They found that

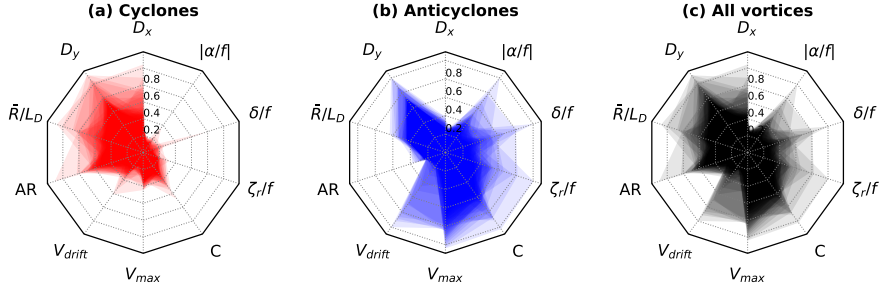


Figure 14: Multivariate distributions of all statistical parameters for all vortices, separated by vortex sense. Zonal-mean zonal wind is omitted since that is unique to the GCM and is not strictly a vortex characteristic. Each axis contains the absolute-normalised values such that each parameter varies between 0 and 1. Colour opacity reflects the number density of vortices along each axis (more transparent colours means fewer vortices exhibit that value). The sequence of parameters is in no particular order.

807 the value of the Burger number strongly determines the configuration of polar  
 808 vortices, with small values ( $1 - 1.7 \times 10^{-4}$ ) corresponding to a jovian configura-  
 809 tion of multiple, small, and often circumpolar vortices, with a transition region  
 810 followed by a kronian regime ( $1.4 \times 10^{-3}$ ) and a general regime of the Ice Giants  
 811 ( $1 - 7 \times 10^{-2}$ ), both with a much stronger, pole-centred, and stable cyclone.

812 Using the Rossby deformation radius inferred in Section 2.5 and the mean  
 813 planetary radius of Saturn,  $a = 58232$  km, gives estimates of Burger number of  
 814  $1.9 - 2.3 \times 10^{-4}$  beyond  $\pm 60^\circ$ . This is directly comparable to the jovian regime  
 815 identified by Brueshaber et al. (2019), half that of the transition region, and  
 816 one eighth that of the kronian regime.

817 Inspecting the polar regions of the GCM through the many cycles of quies-  
 818 cence and disruption, it is clear that the Saturn-DYNAMICO model actually  
 819 exhibits all of the polar vortex configurations identified by Brueshaber et al.  
 820 (2019), despite the slowly-varying zonal flow with time. However, using this  
 821 formula the theory predicts that the Burger number regimes of (Brueshaber  
 822 et al., 2019) greater than jovian should not occur on Saturn at all, despite the  
 823 clear variability in Saturn-DYNAMICO vortex configurations. They show that

824 the vortex configuration is strongly determined by the Burger number, but we  
825 see here that the configuration may in fact vary weakly with Burger regime in  
826 the DYNAMICO GCM. From this work, their values of Burger number seem  
827 too high, and those magnitudes do not allow for a commensurate change in vor-  
828 tex configuration. We believe this points to key differences between the global  
829 resolution of eddy-to-mean interactions of DYNAMICO, and the idealised po-  
830 lar simulations of (Brueshaber et al., 2019). In addition, perhaps the picture  
831 is more subtle or complex, such that defining vortex configuration regimes by  
832 Burger number incompletely captures the details of the relationship between  
833 the two.

#### 834 4. Conclusions

835 Large-scale vortices in the Saturn-DYNAMICO GCM occur spontaneously  
836 in the model as a result of well-resolved eddy-to-mean interactions. While the  
837 spatial, temporal, and dynamical trends are broadly consistent with the historic  
838 record of vortices on the giant planets, there are still important differences  
839 that are explainable and present the opportunity for future exploration through  
840 modelling and comparison to observations.

##### 841 4.1. Strengths and limitations of the methods

842 The manual method has necessarily limited temporal sampling compared to  
843 the automated methods, but seems to be as reliable as observational studies.  
844 However, despite the benefits of improved assumptions, a direct sense of the  
845 vorticity field, and multiple modelled Saturn years, the result still does not ac-  
846 cord with the some expectations of giant planet vortices (most importantly, the  
847 lack of a clear vortex-sense asymmetry in vortex shape). This could come from  
848 multiple sources; a statistical effect due to the small sample size, flawed input as-  
849 sumptions, inherent uncertainty in human-visual detection, inherent differences  
850 between the model and the planets, or other unknown sources (making statisti-  
851 cal conclusions difficult). Regardless, since there is a similar lack of vortex-sense

852 asymmetry in previous observational studies, we conclude that we must share  
853 the same limitations and biases as those studies. This method is best used with  
854 sparse planetary imaging datasets or short model timescales, but is considered  
855 less robust than the dynamical method in the latter case.

856 Since the neural network is trained with the results of the manual method, it  
857 is necessarily constrained by the same assumptions, and despite its highly non-  
858 linear pattern recognition it can only search for things that look like manually-  
859 detected vortices. The benefit to this approach is that the algorithm can be  
860 applied to the entire time series of model outputs and can incorporate in its  
861 detection the thermal and dynamical fields simultaneously. During network op-  
862 timisation, we found that the optimal configuration is the one with the least  
863 complexity, implying that the problem could be simpler than initially expected.  
864 From the feature analysis, we found that temperature correlates the most to  
865 the positive classification of a “vortex”, so it may still be possible to perform  
866 this kind of analysis only with that variable. This has positive implications for  
867 future work which will include a deeper exploration of the network configuration  
868 and detection algorithm in the context of planetary imaging datasets and re-  
869 trieved thermal fields. This method is very useful if one has confidence in their  
870 manually-detected vortices and wants to apply them as a training set to a larger  
871 time series of similar data (observational data, retrievals, or model outputs).

872 The most glaring issue with the ANN method is that it massively over-  
873 estimates the number of vortices with respect to the other two methods. While  
874 many of the detected vortices were well-captured on inspection, this method  
875 clearly detects many more vorticity features that escaped the human eye and the  
876 dynamical constraints of AMEDA. The architecture performs well with respect  
877 to performance metrics, so it could be that the ANN vortices were simply weak  
878 enough to fall within the visual uncertainties of the manual method (evident in  
879 the ANN distribution of vortex intensity), or it was difficult to satisfy the spatial  
880 or dynamical constraints of AMEDA for these vortices. We emphasize that this  
881 neural network approach is a proof-of-concept and despite this positive early  
882 implementation, there is still work to be done in growing the training set and

883 improving the architecture for vortex detection.

884 Unlike the other two methods, the dynamical approach using AMEDA is “in-  
885 telligent” – it requires some physical assumptions but applies physical equations  
886 directly with the dynamical fields to extract the physical and dynamical proper-  
887 ties of vortices. Developed for terrestrial oceanography, it robustly captures the  
888 centres and boundaries of eddies and vortices, but is strongly sensitive to the  
889 assumptions of Rossby deformation radius and struggles in strongly-disrupted  
890 regions. Although this method can not be used for imaging observations like  
891 the others, it does have potential use with thermal retrievals and it is excellent  
892 for analysing modelled dynamical fields of any temporal cadence, can be used in  
893 global or regional applications, and can be adapted for other planetary bodies.  
894 The Okubo-Weiss parameter and the dynamical terms that comprise it have  
895 proven to be a very helpful diagnostic tool in understanding and separating the  
896 dynamical behaviour of cyclones and anticyclones in the model fields. Having  
897 been applied to dynamical observations of terrestrial oceans and now the mod-  
898 elled Saturn atmosphere, there is a potential use case in giant planets whose  
899 horizontal wind field is well-resolved (e.g. through high resolution photometry  
900 and cloud-tracking).

901 Dynamical models like AMEDA show the great opportunity to gain  
902 useful insights into atmospheric dynamics in cases when machine learn-  
903 ing techniques are not applicable. The machine learning model described  
904 here (which is purely data-driven) is in fact a totally different approach  
905 to AMEDA. Sophisticated approaches are emerging that combine the  
906 benefits of equation-driven models with the computational and statisti-  
907 cal benefits of machine learning, so called Physics-Informed Neural Networks  
908 ([PINNs Raissi et al., 2019](#); [Bihlo and Popovych, 2022](#); [Li et al., 2023](#); [Sharma et al., 2023](#); [Kumar et al., 2024](#)  
909 , for atmospheric modelling across many sectors. Future operational monitoring  
910 of planetary atmospheres could benefit greatly from such an inter-disciplinary  
911 application of these techniques.

912 Importantly, each method presented here does sometimes give slightly differ-  
913 ent answers, and occasionally there are large discrepancies that are still unex-

914 plained. Sometimes there are features that the eye quite easily determines to be  
915 a vortex, but AMEDA does not strictly find a closed streamline about a point  
916 of maximum angular momentum that also passes the Rossby-scale filter. Other  
917 times AMEDA might quite easily find many features that satisfy this condition,  
918 but that the human eye would not readily classify as vortex, if indeed it is per-  
919 ceived at all with the given map contrast. Each method has particular use cases  
920 and should be chosen according to the specific requirements of the analysis.

#### 921 *4.2. Agreement with observations*

922 All methods broadly reproduce the observed vortex distributions of previous  
923 studies. We do not find any long term variability with seasonal changes in solar  
924 insolation or mean atmospheric temperature. Vortices only form at the highest  
925 latitude westward jets, where the barotropic instability criterion is frequently  
926 violated, suggesting that barotropic instability is a necessary condition for cy-  
927 clogenesis. There is an overall trend towards smaller and more circular vortices,  
928 with a meridional correlation with the Rossby deformation radius, implying  
929 mutual geostrophic adjustment of eddy fronts and vortex boundaries.

930 By comparing spatial structure and internal dynamics we confirm that the  
931 largest vortices are more rotation-dominated than smaller vortices, allowing  
932 them to be more long-lived and stable (and indeed these vortices are present in  
933 all model epochs independent of eddy-burst events). Cyclones are more spatially  
934 diverse, often being quite zonally-oblate (like the dark cyclonic circulations ob-  
935 served in the atmospheres of Jupiter and Saturn) while anticyclones are almost  
936 always circular (like the bright white spots on Jupiter and Saturn). Anticyclones  
937 are far more dynamically diverse, exhibiting greater ranges and magnitudes of  
938 edge velocity, vorticity, divergence, and lateral strain, and lying further from  
939 the pure shear regime than comparably large cyclones. Anticyclones are the  
940 strongest vortices in the model and cyclones are never more than half as intense  
941 as the strongest anticyclone, potentially reflecting the fundamental dynamical  
942 asymmetry in sign-selection.

943 *4.3. Disagreement with observations*

944 The most important differences between the modelled and observed vortices  
945 are in the distributions of vortex location and concentration, size, and intensity.  
946 Nearby zonal wind conditions seem to be the main driver of vortical structures in  
947 the GCM. The magnitudes of zonal wind affect the internal and edge dynamics  
948 of the vortices, and the shape of the zonal wind profile affects their formation  
949 rate and size.

950 The non-detection of vortices below  $\pm 60^\circ$  latitude could reflect the decreased  
951 spatial resolution of the model at low and mid latitudes, but is more likely to be  
952 due to the perennial barotropic stability of the flow at these latitudes. Larger  
953 zonal jet spacing results in larger shear zones which can produce vortices that  
954 are much larger than in observations (even if the overall size trends are similar).  
955 In addition, even with the inherent asymmetric sign selection, a cyclonic bias in  
956 concentration remains due to the cyclonic shear zones in the model being simply  
957 larger than anticyclonic shear zones. A more realistic jet structure (smaller jet  
958 spacing, more jets, less barotropic stability) would likely produce vortices that  
959 resemble more closely observations. Finally, the model lacks moist convection  
960 which can modify vortices in terms of spatial structure and dynamical behaviour  
961 (O'Neill et al., 2015), but also their very formation (because we showed that jet  
962 structure influence vortices).

963 *4.4. Future work*

964 The DYNAMICO model often exhibits features and characteristics of all the  
965 giant planets at different times. This could point to fundamental differences in  
966 dynamical regimes in the atmospheres of the giant planets. A particularly in-  
967 teresting experiment will be to investigate how the planetary Burger number  
968 correlates to the configuration of the polar vortices as a function of time. The  
969 potential implications are that the giant planets themselves may go through  
970 their own periods of variability in Burger number and polar vortex configura-  
971 tion, and the DYNAMICO GCM will be valuable tool to further explore this  
972 connection.

973 A quantitative exploration of vortex lifetime and merging/splitting events  
974 may provide useful insights into the relationship between the dynamics of the  
975 mean flow and the development cycle of large-scale vortices, particularly asso-  
976 ciated with large-scale eddy-burst events. Identifying the important dynamical  
977 drivers of vortex generation and dissipation on the synoptic scale in comparison  
978 to observations would reveal the dynamical mechanisms that are well-captured  
979 in the model and could highlight areas of further study of GCM vortices.

980 The conclusions of [Boissinot et al. \(2024\)](#) suggest that moist convection  
981 is required to produce a more realistic jet structure and [O'Neill et al. \(2015\)](#)  
982 suggest the release of latent heat during moist convection is crucial for accurately  
983 representing cyclogenesis. When combined with the conclusions of this work, we  
984 raise the question of whether moist convection is required directly to produce  
985 more realistic vortices. We speculate here that these vortex distributions may  
986 be only indirectly linked to GCM configuration (moist convection, model depth,  
987 vertical resolution), such that vortex distributions will be simply as realistic as  
988 the zonal jet structure. These methodologies can be applied to the simulations  
989 of [Boissinot et al. \(2024\)](#) that include the resolution of moist convection on an  
990 extended vertical grid in multiple moist convection schemes (and their associated  
991 zonal jet structures).

## 992 **Acknowledgments**

993 The authors thank the Editor Julianne Moses and both anonymous review-  
994 ers for extremely constructive reviews which helped to improve the manuscript.  
995 The authors acknowledge the exceptional computing support from Grand  
996 Equipement National de Calcul Intensif (GENCI) and Centre Informatique Na-  
997 tional de l'Enseignement Supérieur (CINES). All the simulations presented here  
998 were carried out on the Occigen cluster hosted at CINES.

999 Donnelly, Spiga, and Guerlet acknowledge funding from Agence Nationale  
1000 de la Recherche (ANR), project EMERGIANT ANR-17-CE31-0007, James  
1001 was supported by Science and Technology Facilities Council (STFC) grant



1002 ST/W00089X/1, and Bardet was supported by a European Research Coun-  
1003 cil Consolidator Grant (under the European Union's Horizon 2020 research and  
1004 innovation program, grant agreement No 723890).

## 1005 5. Data availability

1006 The data used in this study are fully open and available for public ac-  
1007 cess. All the simulations presented in this paper were carried out on the  
1008 (now defunct) Occigen cluster hosted at CINES and are stored on the ADAS-  
1009 TRA cluster hosted at CINES. This work was granted access to the High-  
1010 Performance Computing (HPC) resources of CINES under the allocations  
1011 2015-017357, 2016-017548, A001-0107548, A003-0107548, and A004-0110391  
1012 made by GENCI. Processed data can be provided upon request. All code  
1013 used for post-processing and generation of figures is available on GitHub at  
1014 [https://github.com/PTDonnelly/dynamico\\_gcm](https://github.com/PTDonnelly/dynamico_gcm).

## 1015 References

- 1016 Adriani, A., Bracco, A., Grassi, D., Moriconi, M.L., Mura, A., Orton, G., Al-  
1017 tieri, F., Ingersoll, A., Atreya, S.K., Lunine, J.I., Migliorini, A., Noschese, R.,  
1018 Cicchetti, A., Sordini, R., Tosi, F., Sindoni, G., Plainaki, C., Dinelli, B.M.,  
1019 Turrini, D., Filacchione, G., Piccioni, G., Bolton, S.J., 2020. Two-year obser-  
1020 vations of the Jupiter polar regions by JIRAM on board Juno. *Journal of Geo-*  
1021 *physical Research: Planets* 125, e2019JE006098. doi:10.1029/2019JE006098.
- 1022 Adriani, A., Moriconi, M.L., Altieri, F., Sindoni, G., Ingersoll, A.P., Grassi, D.,  
1023 Mura, A., Atreya, S.K., Orton, G., Lunine, J.I., Fletcher, L.N., Simon, A.A.,  
1024 Melin, H., Tosi, F., Cicchetti, A., Noschese, R., Sordini, R., Levin, S., Bolton,  
1025 J., Plainaki, C., Olivieri, A., 2018. Characterization of Mesoscale Waves in  
1026 the Jupiter NEB by Jupiter InfraRed Auroral Mapper on board Juno. *The*  
1027 *Astronomical Journal* 156, 246. doi:10.3847/1538-3881/aae525.

- 1028 Antuñano, A., del Río-Gaztelurrutia, T., Sánchez-Lavega, A., Rodríguez-  
1029 Aseguinolaza, J., 2018. Cloud morphology and dynamics in Saturn's northern  
1030 polar region. *Icarus* 299, 117–132. doi:[10.1016/j.icarus.2017.07.017](https://doi.org/10.1016/j.icarus.2017.07.017).
- 1031 Antuñano, A., Río-Gaztelurrutia, T., Sánchez-Lavega, A., Hueso, R., 2015. Dy-  
1032 namics of Saturn's polar regions. *Journal of Geophysical Research (Planets)*  
1033 120, 155–176. doi:[10.1002/2014JE004709](https://doi.org/10.1002/2014JE004709).
- 1034 Baines, K.H., Momary, T.W., Fletcher, L.N., Showman, A.P., Roos-Serote, M.,  
1035 Brown, R.H., Buratti, B.J., Clark, R.N., Nicholson, P.D., 2009. Saturn's  
1036 north polar cyclone and hexagon at depth revealed by Cassini/VIMS. *Plan.*  
1037 & *Space Sci.* 57, 1671–1681. doi:[10.1016/j.pss.2009.06.026](https://doi.org/10.1016/j.pss.2009.06.026).
- 1038 Balwada, D., Xiao, Q., Smith, S., Abernathey, R., Gray, A.R., 2021. Ver-  
1039 tical fluxes conditioned on vorticity and strain reveal submesoscale venti-  
1040 lation. *Journal of Physical Oceanography* 51, 2883 – 2901. doi:[10.1175/  
1041 JPO-D-21-0016.1](https://doi.org/10.1175/JPO-D-21-0016.1).
- 1042 Bardet, D., Spiga, A., Guerlet, S., Cabanes, S., Millour, E., Boissinot, A., 2021.  
1043 Global climate modeling of Saturn's atmosphere. Part IV: Stratospheric equa-  
1044 torial oscillation. *Icarus* 354, 114042. doi:[10.1016/j.icarus.2020.114042](https://doi.org/10.1016/j.icarus.2020.114042).
- 1045 Bihlo, A., Popovych, R.O., 2022. Physics-informed neural networks for the  
1046 shallow-water equations on the sphere. *Journal of Computational Physics*  
1047 456, 111024. doi:<https://doi.org/10.1016/j.jcp.2022.111024>.
- 1048 Blake, J.S.D., Fletcher, L.N., Orton, G.S., Antuñano, A., Roman, M.T.,  
1049 Kasaba, Y., Fujiyoshi, T., Melin, H., Bardet, D., Sinclair, J.A., Es-Sayeh,  
1050 M., 2023. Saturn's seasonal variability from four decades of ground-based  
1051 mid-infrared observations. *Icarus* 392, 115347. doi:[10.1016/j.icarus.2022.  
1052 115347](https://doi.org/10.1016/j.icarus.2022.115347).
- 1053 Boissinot, A., Spiga, A., Guerlet, S., Cabanes, S., Bardet, D., 2024. Global  
1054 climate modeling of the Jupiter troposphere and effect of dry and moist con-  
1055 vection on jets. *AA* 687, A274. doi:[10.1051/0004-6361/202245220](https://doi.org/10.1051/0004-6361/202245220).

- 1056 Bolton, S.J., Levin, S.M., Guillot, T., Li, C., Kaspi, Y., Orton, G., Wong, M.H.,  
1057 Oyafuso, F., Allison, M., Arballo, J., Atreya, S., Becker, H.N., Bloxham, J.,  
1058 Brown, S.T., Fletcher, L.N., Galanti, E., Gulkis, S., Janssen, M., Ingersoll,  
1059 A., Lunine, J.L., Misra, S., Steffes, P., Stevenson, D., Waite, J.H., Yadav,  
1060 R.K., Zhang, Z., 2021. Microwave observations reveal the deep extent and  
1061 structure of Jupiter's atmospheric vortices. *Science* 374, 968–972. doi:[10.1126/science.abf1015](https://doi.org/10.1126/science.abf1015).  
1062
- 1063 Bouchet, F., Nardini, C., Tangarife, T., 2013. Kinetic Theory of Jet Dynamics  
1064 in the Stochastic Barotropic and 2D Navier-Stokes Equations. *Journal of*  
1065 *Statistical Physics* 153, 572–625. doi:[10.1007/s10955-013-0828-3](https://doi.org/10.1007/s10955-013-0828-3).
- 1066 Bouchet, F., Simonnet, E., 2009. Random Changes of Flow Topology in  
1067 Two-Dimensional and Geophysical Turbulence. *Physical Review Letters* 102,  
1068 094504. doi:[10.1103/PhysRevLett.102.094504](https://doi.org/10.1103/PhysRevLett.102.094504).
- 1069 Brueshaber, S.R., Sayanagi, K.M., Dowling, T.E., 2019. Dynamical regimes of  
1070 giant planet polar vortices. *Icarus* 323, 46–61. doi:[10.1016/j.icarus.2019.02.001](https://doi.org/10.1016/j.icarus.2019.02.001).  
1071
- 1072 Cabanes, S., Aurnou, J., Favier, B., Le Bars, M., 2017. A laboratory model for  
1073 deep-seated jets on the gas giants. *Nature Physics* 13, 387–390. doi:[10.1038/nphys4001](https://doi.org/10.1038/nphys4001).  
1074
- 1075 Cabanes, S., Spiga, A., Young, R.M.B., 2020. Global climate modeling of Sat-  
1076 urn's atmosphere. Part III: Global statistical picture of zonostrophic tur-  
1077 bulence in high-resolution 3d-turbulent simulations. *Icarus* 345, 113705.  
1078 doi:[10.1016/j.icarus.2020.113705](https://doi.org/10.1016/j.icarus.2020.113705).
- 1079 Caldwell, J., Hua, X.M., Turgeon, B., Westphal, J.A., Barnet, C.D., 1993. The  
1080 drift of Saturn's north polar spot observed by the Hubble Space Telescope.  
1081 *Science* 260, 326–329. doi:[10.1126/science.260.5106.326](https://doi.org/10.1126/science.260.5106.326).
- 1082 Chaigneau, A., Gizolme, A., Grados, C., 2008. Mesoscale eddies off Peru in al-

- 1083 timeter records: Identification algorithms and eddy spatio-temporal patterns.  
1084 Prog. Oceanogr. 79, 106–119. doi:[10.1016/j.pocean.2008.10.013](https://doi.org/10.1016/j.pocean.2008.10.013).
- 1085 Chelton, D.B., Schlax, M.G., Samelson, R.M., de Szoeke, R.A., 2007. Global  
1086 observations of large oceanic eddies. Geophys. Res. Lett. 34, L15606. doi:[10.](https://doi.org/10.1029/2007GL030812)  
1087 [1029/2007GL030812](https://doi.org/10.1029/2007GL030812).
- 1088 de Pater, I., Sromovsky, L.A., Fry, P.M., Hammel, H.B., Baranec, C., Sayanagi,  
1089 K.M., 2015. Record-breaking storm activity on Uranus in 2014. Icarus 252,  
1090 121–128. doi:[10.1016/j.icarus.2014.12.037](https://doi.org/10.1016/j.icarus.2014.12.037).
- 1091 del Genio, A.D., Achterberg, R.K., Baines, K.H., Flasar, F.M., Read, P.L.,  
1092 Sánchez-Lavega, A., Showman, A.P., 2009. Saturn Atmospheric Structure  
1093 and Dynamics, In: Saturn from Cassini-Huygens. Springer. chapter 6. pp.  
1094 113–159. doi:[10.1007/978-1-4020-9217-6\\_6](https://doi.org/10.1007/978-1-4020-9217-6_6).
- 1095 del Río-Gaztelurrutia, T., Legarreta, J., Hueso, R., Pérez-Hoyos, S., Sánchez-  
1096 Lavega, A., 2010. A long-lived cyclone in Saturn's atmosphere: Observations  
1097 and models. Icarus 209, 665–681. doi:[10.1016/j.icarus.2010.04.002](https://doi.org/10.1016/j.icarus.2010.04.002).
- 1098 del Río-Gaztelurrutia, T., Sánchez-Lavega, A., Antuñano, A., Legarreta, J.,  
1099 García-Melendo, E., Sayanagi, K.M., Hueso, R., Wong, M.H., Pérez-Hoyos,  
1100 S., Rojas, J.F., Simon, A.A., de Pater, I., Blalock, J., Barry, T., 2018. A  
1101 planetary-scale disturbance in a long living three vortex coupled system in  
1102 Saturn's atmosphere. Icarus 302, 499–513. doi:[10.1016/j.icarus.2017.11.](https://doi.org/10.1016/j.icarus.2017.11.029)  
1103 [029](https://doi.org/10.1016/j.icarus.2017.11.029).
- 1104 Dowling, T.E., Ingersoll, A.P., 1989. Jupiter's Great Red Spot as a shallow  
1105 water system. Journal of Atmospheric Sciences 46, 3256–3278. doi:[10.1175/  
1106 1520-0469\(1989\)046<3256:JGRSAA>2.0.CO;2](https://doi.org/10.1175/1520-0469(1989)046<3256:JGRSAA>2.0.CO;2).
- 1107 Dyudina, U.A., Ingersoll, A.P., Ewald, S.P., Vasavada, A.R., West, R.A.,  
1108 Baines, K.H., Momary, T.W., Del Genio, A.D., Barbara, J.M., Porco, C.C.,  
1109 Achterberg, R.K., Flasar, F.M., Simon-Miller, A.A., Fletcher, L.N., 2009.

- 1110 Saturn's south polar vortex compared to other large vortices in the Solar  
1111 System. *Icarus* 202, 240–248. doi:[10.1016/j.icarus.2009.02.014](https://doi.org/10.1016/j.icarus.2009.02.014).
- 1112 Dyudina, U.A., Ingersoll, A.P., Ewald, S.P., Vasavada, A.R., West, R.A., Del  
1113 Genio, A.D., Barbara, J.M., Porco, C.C., Achterberg, R.K., Flasar, F.M.,  
1114 Simon-Miller, A.A., Fletcher, L.N., 2008. Dynamics of Saturn's South Polar  
1115 Vortex. *Science* 319, 1801. doi:[10.1126/science.1153633](https://doi.org/10.1126/science.1153633).
- 1116 Flament, P.J., Kennan, S.C., Knox, R.A., Niiler, P.P., Bernstein, R.L., 1996.  
1117 The three-dimensional structure of an upper ocean vortex in the tropical  
1118 pacific ocean. *Nature* 383, 610–613. doi:[10.1038/383610a0](https://doi.org/10.1038/383610a0).
- 1119 Fletcher, L., Orton, G., Oyafuso, F., Zhang, Z., Brueshaber, S., Wong, M.H., Li,  
1120 C., Mura, A., Grassi, D., Melin, H., Levin, S., Bolton, S., Rogers, J., Brown,  
1121 S., 2022. Juno Characterisation of Cyclonic “Folded Filamentary Regions”  
1122 within Jupiter's North Polar Domain, in: 44th COSPAR Scientific Assembly.  
1123 Held 16-24 July, p. 536.
- 1124 Fletcher, L.N., de Pater, I., Orton, G.S., Hammel, H.B., Sitko, M.L., Irwin,  
1125 P.G.J., 2014. Neptune at summer solstice: Zonal mean temperatures from  
1126 ground-based observations, 2003-2007. *Icarus* 231, 146–167. doi:[10.1016/j.  
1127 icarus.2013.11.035](https://doi.org/10.1016/j.icarus.2013.11.035).
- 1128 Fletcher, L.N., Irwin, P.G.J., Orton, G.S., Teanby, N.A., Achterberg, R.K.,  
1129 Bjoraker, G.L., Read, P.L., Simon-Miller, A.A., Howett, C., de Kok, R.,  
1130 Bowles, N., Calcutt, S.B., Hesman, B., Flasar, F.M., 2008. Temperature and  
1131 Composition of Saturn's Polar Hot Spots and Hexagon. *Science* 319, 79–81.  
1132 doi:[10.1126/science.1149514](https://doi.org/10.1126/science.1149514).
- 1133 Fletcher, L.N., King, O.R.T., Harkett, J., Hammel, H.B., Roman, M.T.,  
1134 Melin, H., Hedman, M.M., Moses, J.I., Guerlet, S., Milam, S.N.,  
1135 Tiscareno, M.S., 2023. Saturn's atmosphere in northern summer  
1136 revealed by jwst/miri. *Journal of Geophysical Research: Planets*  
1137 128, e2023JE007924. doi:<https://doi.org/10.1029/2023JE007924>,

- 1138 [arXiv:https://agupubs.onlinelibrary.wiley.com/doi/pdf/10.1029/2023JE007924](https://agupubs.onlinelibrary.wiley.com/doi/pdf/10.1029/2023JE007924).  
1139 e2023JE007924 2023JE007924.
- 1140 Fletcher, L.N., Orton, G.S., Rogers, J.H., Giles, R.S., Payne, A.V., Irwin,  
1141 P.G.J., Vedovato, M., 2017a. Moist convection and the 2010-2011 revival of  
1142 Jupiter's South Equatorial Belt. *Icarus* 286, 94–117. doi:[10.1016/j.icarus.](https://doi.org/10.1016/j.icarus.2017.01.001)  
1143 [2017.01.001](https://doi.org/10.1016/j.icarus.2017.01.001).
- 1144 Fletcher, L.N., Orton, G.S., Rogers, J.H., Simon-Miller, A.A., de Pater, I.,  
1145 Wong, M.H., Mousis, O., Irwin, P.G.J., Jacquesson, M., Yanamandra-Fisher,  
1146 P.A., 2011. Jovian temperature and cloud variability during the 2009-2010  
1147 fade of the South Equatorial Belt. *Icarus* 213, 564–580. doi:[10.1016/j.](https://doi.org/10.1016/j.icarus.2011.03.007)  
1148 [icarus.2011.03.007](https://doi.org/10.1016/j.icarus.2011.03.007).
- 1149 Fletcher, L.N., Orton, G.S., Sinclair, J.A., Donnelly, P., Melin, H., Rogers, J.H.,  
1150 Greathouse, T.K., Kasaba, Y., Fujiyoshi, T., Sato, T.M., Fernandes, J., Irwin,  
1151 P.G.J., Giles, R.S., Simon, A.A., Wong, M.H., Vedovato, M., 2017b. Jupiter's  
1152 North Equatorial Belt expansion and thermal wave activity ahead of Juno's  
1153 arrival. *Geophys. Res. Lett.* 44, 7140–7148. doi:[10.1002/2017GL073383](https://doi.org/10.1002/2017GL073383).
- 1154 Fletcher, L.N., Orton, G.S., Yanamandra-Fisher, P., Fisher, B.M., Parrish, P.D.,  
1155 Irwin, P.G.J., 2009. Retrievals of atmospheric variables on the gas giants  
1156 from ground-based mid-infrared imaging. *Icarus* 200, 154–175. doi:[10.1016/](https://doi.org/10.1016/j.icarus.2008.11.019)  
1157 [j.icarus.2008.11.019](https://doi.org/10.1016/j.icarus.2008.11.019).
- 1158 Galanti, E., Kaspi, Y., Miguel, Y., Guillot, T., Durante, D., Racioppa, P., Iess,  
1159 L., 2019. Saturn's deep atmospheric flows revealed by the cassini grand finale  
1160 gravity measurements. *Geophysical Research Letters* 46, 616–624. doi:[10.](https://doi.org/10.1029/2018GL078087)  
1161 [1029/2018GL078087](https://doi.org/10.1029/2018GL078087).
- 1162 García-Melendo, E., Sánchez-Lavega, A., Legarreta, J., Perez-Hoyos, S., Hueso,  
1163 R., 2010. A strong high altitude narrow jet detected at Saturn's equator.  
1164 *Geophys. Res. Lett.* 37, L22204. doi:[10.1029/2010GL045434](https://doi.org/10.1029/2010GL045434).

- 1165 García-Melendo, E., Sánchez-Lavega, A., Hueso, R., 2007. Numerical models  
1166 of Saturn's long-lived anticyclones. *Icarus* 191, 665–677. doi:[10.1016/j.  
1167 icarus.2007.05.020](https://doi.org/10.1016/j.icarus.2007.05.020).
- 1168 Gastine, T., Wicht, J., Duarte, L.D.V., Heimpel, M., Becker, A., 2014. Ex-  
1169 plaining Jupiter's magnetic field and equatorial jet dynamics. *Geophysical  
1170 Research Letters* 41, 5410–5419. doi:[10.1002/2014GL060814](https://doi.org/10.1002/2014GL060814).
- 1171 Grassi, D., Adriani, A., Moriconi, M.L., Mura, A., Tabataba-Vakili, F., In-  
1172 gersoll, A., Orton, G., Hansen, C., Altieri, F., Filacchione, G., Sindoni, G.,  
1173 Dinelli, B.M., Fabiano, F., Bolton, S.J., Levin, S., Atreya, S.K., Lunine, J.I.,  
1174 Momary, T., Tosi, F., Migliorini, A., Piccioni, G., Noschese, R., Cicchetti,  
1175 A., Plainaki, C., Olivieri, A., Turrini, D., Stefani, S., Sordini, R., Amoroso,  
1176 M., 2018. First Estimate of Wind Fields in the Jupiter Polar Regions From  
1177 JIRAM-Juno Images. *Journal of Geophysical Research: Planets* 123, 1511–  
1178 1524. doi:[10.1029/2018JE005555](https://doi.org/10.1029/2018JE005555).
- 1179 Guerlet, S., Spiga, A., Sylvestre, M., Indurain, M., Fouchet, T., Leconte, J.,  
1180 Millour, E., Wordsworth, R., Capderou, M., Bézard, B., Forget, F., 2014.  
1181 Global climate modeling of Saturn's atmosphere. Part I: Evaluation of the  
1182 radiative transfer model. *Icarus* 238, 110–124. doi:[10.1016/j.icarus.2014.  
1183 05.010](https://doi.org/10.1016/j.icarus.2014.05.010).
- 1184 Guillot, T., Miguel, Y., Militzer, B., Hubbard, W.B., Kaspi, Y., Galanti, E.,  
1185 Cao, H., Helled, R., Wahl, S.M., Iess, L., Folkner, W.M., Stevenson, D.J.,  
1186 Lunine, J.I., Reese, D.R., Biekman, A., Parisi, M., Durante, D., Connerney,  
1187 J.E.P., Levin, S.M., Bolton, S.J., 2018. A suppression of differential rotation  
1188 in Jupiter's deep interior. *Nature* 555, 227–230. doi:[10.1038/nature25775](https://doi.org/10.1038/nature25775).
- 1189 Hanel, R., Conrath, B., Flasar, F.M., Kunde, V., Maguire, W., Pearl, J., Pir-  
1190 raglia, J., Samuelson, R., Cruikshank, D., Gautier, D., Gierasch, P., Horn,  
1191 L., Ponnampereuma, C., 1982. Infrared observations of the Saturnian system  
1192 from Voyager 2. *Science* 215, 544–548. doi:[10.1126/science.215.4532.544](https://doi.org/10.1126/science.215.4532.544).

- 1193 Hanel, R., Conrath, B., Flasar, F.M., Kunde, V., Maguire, W., Pearl, J.C., Pir-  
1194 raglia, J., Samuelson, R., Herath, L., Allison, M., Cruikshank, D.P., Gautier,  
1195 D., Gierasch, P.J., Horn, L., Koppany, R., Ponnampereuma, C., 1981. Infrared  
1196 observations of the Saturnian system from Voyager 1. *Science* 212, 192–200.  
1197 doi:[10.1126/science.212.4491.192](https://doi.org/10.1126/science.212.4491.192).
- 1198 Heimpel, M., Aurnou, J., Wicht, J., 2005. Simulation of equatorial and high-  
1199 latitude jets on Jupiter in a deep convection model. *Nature* 438, 193–196.  
1200 doi:[10.1038/nature04208](https://doi.org/10.1038/nature04208).
- 1201 Heimpel, M., Gastine, T., Wicht, J., 2016. Simulation of deep-seated zonal jets  
1202 and shallow vortices in gas giant atmospheres. *Nature Geoscience* 9, 19–23.  
1203 doi:[10.1038/ngeo2601](https://doi.org/10.1038/ngeo2601).
- 1204 Heimpel, M., Gómez Pérez, N., 2011. On the relationship between zonal jets  
1205 and dynamo action in giant planets. *Geophysical Research Letters* 38, L14201.  
1206 doi:[10.1029/2011GL047562](https://doi.org/10.1029/2011GL047562).
- 1207 Holmes, R.M., Thomas, L.N., Thompson, L., Darr, D., 2014. Potential vorticity  
1208 dynamics of tropical instability vortices. *Journal of Physical Oceanography*  
1209 44, 995 – 1011. doi:[10.1175/JPO-D-13-0157.1](https://doi.org/10.1175/JPO-D-13-0157.1).
- 1210 Holton, J., 2004. *An Introduction to Dynamic Meteorology*. Academic press.
- 1211 Hoskins, B.J., Bretherton, F.P., 1972. Atmospheric frontogenesis models: Math-  
1212 ematical formulation and solution. *Journal of Atmospheric Sciences* 29, 11 –  
1213 37. doi:[10.1175/1520-0469\(1972\)029<0011:AFMMFA>2.0.CO;2](https://doi.org/10.1175/1520-0469(1972)029<0011:AFMMFA>2.0.CO;2).
- 1214 Hueso, R., Iñurriagarro, P., Sánchez-Lavega, A., Foster, C.R., Rogers, J.H., Or-  
1215 ton, G.S., Hansen, C., Eichstädt, G., Ordonez-Etxeberria, I., Rojas, J.F.,  
1216 Brueshaber, S.R., Sanz-Requena, J.F., Pérez-Hoyos, S., Wong, M.H., Mo-  
1217 mary, T.W., Jónsson, B., Antuñano, A., Baines, K.H., Dahl, E.K., Mizu-  
1218 moto, S., Go, C., Anguiano-Arteaga, A., 2022. Convective storms in closed  
1219 cyclones in Jupiter’s South Temperate Belt: (I) observations. *Icarus* 380,  
1220 114994. doi:[10.1016/j.icarus.2022.114994](https://doi.org/10.1016/j.icarus.2022.114994).



- 1221 Ingersoll, A.P., Atreya, S., Bolton, S.J., Brueshaber, S., Fletcher, L.N., Levin,  
1222 S.M., Li, C., Li, L., Lunine, J.I., Orton, G.S., Waite, H., 2021. Jupiter's over-  
1223 turning circulation: Breaking waves take the place of solid boundaries. *Geo-*  
1224 *physical Research Letters* 48, e2021GL095756. doi:[10.1029/2021GL095756](https://doi.org/10.1029/2021GL095756).
- 1225 Ingersoll, A.P., Beebe, R.F., Collins, S.A., Hunt, G.E., Mitchell, J.L., Muller,  
1226 P., Smith, B.A., Terrile, R.J., 1979. Zonal velocity and texture in the jovian  
1227 atmosphere inferred from Voyager images. *Nature* 280, 773–775. doi:[10.](https://doi.org/10.1038/280773a0)  
1228 [1038/280773a0](https://doi.org/10.1038/280773a0).
- 1229 Ingersoll, A.P., Beebe, R.F., Mitchell, J.L., Garneau, G.W., Yagi, G.M., Muller,  
1230 J., 1981. Interaction of eddies and mean zonal flow on Jupiter as inferred from  
1231 Voyager 1 and 2 images. *Journal of Geophysical Research* 86, 8733–8743.  
1232 doi:[10.1029/JA086iA10p08733](https://doi.org/10.1029/JA086iA10p08733).
- 1233 Ingersoll, A.P., Dowling, T.E., Gierasch, P.J., Orton, G.S., Read, P.L., Sánchez-  
1234 Lavega, A., Showman, A.P., Simon-Miller, A.A., Vasavada, A.R., 2004. Dy-  
1235 namics of Jupiter's atmosphere. *Jupiter. The Planet, Satellites and Magne-*  
1236 *tosphere*. pp. 105–128.
- 1237 Isern-Fontanet, J., García-Ladona, E., Font, J., 2003. Identification of marine  
1238 eddies from altimetric maps. *J. Atmos. Oceanic Technol.* 20, 772–778. doi:[10.](https://doi.org/10.1175/1520-0426(2003)20<772:IOMEFA>2.0.CO;2)  
1239 [1175/1520-0426\(2003\)20<772:IOMEFA>2.0.CO;2](https://doi.org/10.1175/1520-0426(2003)20<772:IOMEFA>2.0.CO;2).
- 1240 Iñurrigarro, P., Hueso, R., Legarreta, J., Sánchez-Lavega, A., Eichstädt, G.,  
1241 Rogers, J.H., Orton, G.S., Hansen, C.J., Pérez-Hoyos, S., Rojas, J.F., Gómez-  
1242 Forrellad, J.M., 2020. Observations and numerical modelling of a convective  
1243 disturbance in a large-scale cyclone in Jupiter's South Temperate Belt. *Icarus*  
1244 336, 113475. doi:[10.1016/j.icarus.2019.113475](https://doi.org/10.1016/j.icarus.2019.113475).
- 1245 James, M.K., Imber, S.M., Raines, J.M., Yeoman, T.K., Bunce, E.J., 2020. A  
1246 Machine Learning Approach to Classifying MESSENGER FIPS Proton Spec-  
1247 tra. *Journal of Geophysical Research: Space Physics* 125, e2019JA027352.  
1248 doi:[10.1029/2019JA027352](https://doi.org/10.1029/2019JA027352).

- 1249 Karkoschka, E., Tomasko, M., 2005. Saturn's vertical and latitudinal cloud  
1250 structure 1991 - 2004 from HST imaging in 30 filters. *Icarus* 179, 195–221.  
1251 doi:[10.1016/j.icarus.2005.05.016](https://doi.org/10.1016/j.icarus.2005.05.016).
- 1252 Karney, C.F.F., 2012. Algorithms for geodesics. *Journal of Geodesy* 87, 43–55.  
1253 doi:[10.1007/s00190-012-0578-z](https://doi.org/10.1007/s00190-012-0578-z).
- 1254 Kaspi, Y., Flierl, G.R., Showman, A.P., 2009. The deep wind structure of the  
1255 giant planets: Results from an anelastic general circulation model. *Icarus*  
1256 202, 525–542. doi:[10.1016/j.icarus.2009.03.026](https://doi.org/10.1016/j.icarus.2009.03.026).
- 1257 Kaspi, Y., Galanti, E., Hubbard, W.B., Stevenson, D.J., Bolton, S.J., Iess,  
1258 L., Guillot, T., Bloxham, J., Connerney, J.E.P., Cao, H., Durante, D.,  
1259 Folkner, W.M., Helled, R., Ingersoll, A.P., Levin, S.M., Lunine, J.I., Miguel,  
1260 Y., Militzer, B., Parisi, M., Wahl, S.M., 2018. Jupiter's atmospheric  
1261 jet streams extend thousands of kilometres deep. *Nature* 555, 223–226.  
1262 doi:[10.1038/nature25793](https://doi.org/10.1038/nature25793).
- 1263 Kumar, P., Vogel, H., Bruckert, J., Muth, L.J., Hoshyaripour, G.A., 2024. Mieai:  
1264 a neural network for calculating optical properties of internally mixed aerosol  
1265 in atmospheric models. *npj Climate and Atmospheric Science* 7, 110. doi:[10.1038/s41612-024-00652-y](https://doi.org/10.1038/s41612-024-00652-y).
- 1267 Le Vu, B., Stegner, A., Arsouze, T., 2018. Angular Momentum Eddy Detec-  
1268 tion and Tracking Algorithm (AMEDA) and Its Application to Coastal Eddy  
1269 Formation. *Journal of Atmospheric and Oceanic Technology* 35, 739 – 762.  
1270 doi:[10.1175/JTECH-D-17-0010.1](https://doi.org/10.1175/JTECH-D-17-0010.1).
- 1271 Legarreta, J., Sánchez-Lavega, A., 2005. Jupiter's cyclones and anticyclones  
1272 vorticity from Voyager and Galileo images. *Icarus* 174, 178–191. doi:[10.1016/j.icarus.2004.10.006](https://doi.org/10.1016/j.icarus.2004.10.006).
- 1274 Li, B., Hu, Q., Gao, M., Liu, T., Zhang, C., Liu, C., 2023. Physical in-  
1275 formed neural network improving the wrf-chem results of air pollution using

- 1276 satellite-based remote sensing data. *Atmospheric Environment* 311, 120031.  
1277 doi:<https://doi.org/10.1016/j.atmosenv.2023.120031>.
- 1278 Li, C., Ingersoll, A.P., Klipfel, A.P., Brettle, H., 2020. Modeling the stability of  
1279 polygonal patterns of vortices at the poles of Jupiter as revealed by the Juno  
1280 spacecraft. *Proceedings of the National Academy of Sciences* 117, 24082–  
1281 24087. doi:[10.1073/pnas.2008440117](https://doi.org/10.1073/pnas.2008440117).
- 1282 Li, L., Ingersoll, A.P., Vasavada, A.R., Porco, C.C., Del Genio, A.D., Ewald,  
1283 S.P., 2004. Life cycles of spots on Jupiter from Cassini images. *Icarus* 172,  
1284 9–23. doi:[10.1016/j.icarus.2003.10.015](https://doi.org/10.1016/j.icarus.2003.10.015).
- 1285 Li, L., Ingersoll, A.P., Vasavada, A.R., Simon-Miller, A.A., Achterberg, R.K.,  
1286 Ewald, S.P., Dyudina, U.A., Porco, C.C., West, R.A., Flasar, F.M., 2006.  
1287 Waves in Jupiter's atmosphere observed by the Cassini ISS and CIRS instru-  
1288 ments. *Icarus* 185, 416–429. doi:[10.1016/j.icarus.2006.08.005](https://doi.org/10.1016/j.icarus.2006.08.005).
- 1289 Lian, Y., Showman, A.P., 2008. Deep jets on gas-giant planets. *Icarus* 194,  
1290 597–615. doi:[10.1016/j.icarus.2007.10.014](https://doi.org/10.1016/j.icarus.2007.10.014).
- 1291 Lian, Y., Showman, A.P., 2010. Generation of equatorial jets by large-scale  
1292 latent heating on the giant planets. *Icarus* 207, 373–393. doi:[10.1016/j.  
1293 icarus.2009.10.006](https://doi.org/10.1016/j.icarus.2009.10.006).
- 1294 Limaye, S.S., Sromovsky, L.A., 1991. Winds of Neptune - Voyager observations  
1295 of cloud motions. *Journal of Geophysical Research* 96(S01), 18941–18960.  
1296 doi:[10.1029/91JA01701](https://doi.org/10.1029/91JA01701).
- 1297 Liu, J., Schneider, T., 2010. Mechanisms of jet formation on the giant plan-  
1298 ets. *Journal of the Atmospheric Sciences* 67, 3652 – 3672. doi:[10.1175/  
1299 2010JAS3492.1](https://doi.org/10.1175/2010JAS3492.1).
- 1300 Liu, M., Rossby, T., 1993. Observations of the Velocity and Vorticity Structure  
1301 of Gulf Stream Meanders. *Journal of Physical Oceanography* 23, 329 – 345.  
1302 doi:[10.1175/1520-0485\(1993\)023<0329:00TVAV>2.0.CO;2](https://doi.org/10.1175/1520-0485(1993)023<0329:00TVAV>2.0.CO;2).

- 1303 Luszczyk-Cook, S.H., de Pater, I., Ádámkóvics, M., Hammel, H.B., 2010. Seeing  
1304 double at Neptune's south pole. *Icarus* 208, 938–944. doi:[10.1016/j.icarus.  
1305 2010.03.007](https://doi.org/10.1016/j.icarus.2010.03.007).
- 1306 Mac Low, M., Ingersoll, A.P., 1986. Merging of vortices in the atmosphere of  
1307 Jupiter: An analysis of voyager images. *Icarus* 65, 353 – 369. doi:[10.1016/  
1308 0019-1035\(86\)90143-0](https://doi.org/10.1016/0019-1035(86)90143-0).
- 1309 Marcus, P.S., Kundu, T., Lee, C., 2000. Vortex dynamics and zonal flows.  
1310 *Physics of Plasmas* 7, 1630–1640. doi:[10.1063/1.874045](https://doi.org/10.1063/1.874045).
- 1311 Mitchell, J.L., Terrile, R.J., Smith, B.A., Muller, J.P., Ingersoll, A.P., Hunt,  
1312 G.E., Collins, S.A., Beebe, R.F., 1979. Jovian cloud structure and velocity  
1313 fields. *Nature* 280, 776–778. doi:[10.1038/280776a0](https://doi.org/10.1038/280776a0).
- 1314 Mkhinini, N., Coimbra, A., Stegner, A., Arsouze, T., Taupier-Letage, I.,  
1315 Béranger, K., . Long-lived mesoscale eddies in the eastern Mediterranean  
1316 Sea: Analysis of 20 years of AVISO geostrophic velocities. *Journal of Geo-  
1317 physical Research: Oceans* 119, 8603–8626. doi:[10.1002/2014JC010176](https://doi.org/10.1002/2014JC010176).
- 1318 Morales-Juberías, R., Sánchez-Lavega, A., Lecacheux, J., Colas, F., 2002. A  
1319 comparative study of jovian cyclonic features from a six-year (1994–2000)  
1320 survey. *Icarus* 160, 325–335. doi:[10.1006/icar.2002.6973](https://doi.org/10.1006/icar.2002.6973).
- 1321 Morrow, R., Birol, F., Griffin, D., Sudre, J., 2004. Divergent pathways of  
1322 cyclonic and anti-cyclonic ocean eddies. *Geophys. Res. Lett.* 31, L24311.  
1323 doi:[10.1029/2004GL020974](https://doi.org/10.1029/2004GL020974).
- 1324 Niiler, P.P., Maximenko, N.A., Panteleev, G.G., Yamagata, T., Olson, D.B.,  
1325 2003. Near-surface dynamical structure of the Kuroshio Extension. *Journal  
1326 of Geophysical Research: Oceans* 108, 3193. doi:[10.1029/2002JC001461](https://doi.org/10.1029/2002JC001461).
- 1327 Okubo, A., 1970. Horizontal dispersion of floatable particles in the vicinity of  
1328 velocity singularities such as convergences. *Deep-Sea Res. Oceanogr. Abstr.*  
1329 17, 445–454. doi:[10.1016/0011-7471\(70\)90059-8](https://doi.org/10.1016/0011-7471(70)90059-8).

- 1330 Orton, G.S., Antuñaño, A., Fletcher, L.N., Sinclair, J.A., Momary, T.W.,  
1331 Fujiyoshi, T., Yanamandra-Fisher, P., Donnelly, P.T., Greco, J.J., Payne,  
1332 A.V., Boydstun, K.A., Wakefield, L.E., 2022. Unexpected long-term variabil-  
1333 ity in Jupiter's tropospheric temperatures. *Nature Astronomy* 7, 190–197.  
1334 doi:[10.1038/s41550-022-01839-0](https://doi.org/10.1038/s41550-022-01839-0).
- 1335 Orton, G.S., Hansen, C., Caplinger, M., Ravine, M., Atreya, S., Ingersoll, A.P.,  
1336 Jensen, E., Momary, T., Lipkaman, L., Krysak, D., Zimdar, R., Bolton, S.,  
1337 2017. The first close-up images of Jupiter's polar regions: Results from the  
1338 Juno mission JunoCam instrument. *Geophysical Research Letters* 44, 4599–  
1339 4606. doi:<https://doi.org/10.1002/2016GL072443>.
- 1340 Orton, G.S., Sinclair, J., Fletcher, L., Fujiyoshi, T., Yanamandra-Fisher, P.,  
1341 Rogers, J., Irwin, P., Greathouse, T., Seede, R., Simon, J., Nguyen, M., Lai,  
1342 M., 2015. Are Brown Barges the Deserts of the Upper Jovian Atmosphere?,  
1343 in: AAS/Division for Planetary Sciences Meeting Abstracts, p. 502.04.
- 1344 Orton, G.S., Yanamandra-Fisher, P.A., 2005. Saturn's Temperature Field from  
1345 High-Resolution Middle-Infrared Imaging. *Science* 307, 696–698. doi:[10.1126/science.1105730](https://doi.org/10.1126/science.1105730).
- 1347 O'Neill, M.E., Emanuel, K.A., Flierl, G.R., 2015. Polar vortex formation in  
1348 giant-planet atmospheres due to moist convection. *Nature Geoscience* 8, 523–  
1349 526. doi:[10.1038/ngeo2459](https://doi.org/10.1038/ngeo2459).
- 1350 Pérez-Hoyos, S., Sánchez-Lavega, A., French, R.G., Rojas, J.F., 2005. Sat-  
1351 urn's cloud structure and temporal evolution from ten years of Hubble Space  
1352 Telescope images (1994-2003). *Icarus* 176, 155–174. doi:[10.1016/j.icarus.2005.01.014](https://doi.org/10.1016/j.icarus.2005.01.014).
- 1354 Pérez-Hoyos, S., Sanz-Requena, J.F., Barrado-Izagirre, N., Rojas, J.F., Sánchez-  
1355 Lavega, A., IOPW Team, 2012. The 2009-2010 fade of Jupiter's South Equa-  
1356 torial Belt: Vertical cloud structure models and zonal winds from visible  
1357 imaging. *Icarus* 217, 256–271. doi:[10.1016/j.icarus.2011.11.008](https://doi.org/10.1016/j.icarus.2011.11.008).

- 1358 QGIS Development Team, 2022. QGIS Geographic Information System. QGIS  
1359 Association. URL: <https://www.qgis.org>.
- 1360 Raissi, M., Perdikaris, P., Karniadakis, G., 2019. Physics-informed neural net-  
1361 works: A deep learning framework for solving forward and inverse problems  
1362 involving nonlinear partial differential equations. *Journal of Computational*  
1363 *Physics* 378, 686–707. doi:<https://doi.org/10.1016/j.jcp.2018.10.045>.
- 1364 Read, P.L., 2011. Dynamics and circulation regimes of terrestrial planets. *Plan.*  
1365 *& Space Sci.* 59, 900–914. doi:[10.1016/j.pss.2010.04.024](https://doi.org/10.1016/j.pss.2010.04.024).
- 1366 Rogers, J., 1995. *The Giant Planet Jupiter*. Cambridge University Press.
- 1367 Rogers, J.H., 2007. Jupiter embarks on a 'global upheaval'. *Journal of the*  
1368 *British Astronomical Association* 117, 113–115.
- 1369 Rogers, J.H., Mettig, H.J., Adamoli, G., Jacquesson, M., Vedovato, M., 2010.  
1370 Jupiter in 2010: Interim report: Southern hemisphere . URL: [http://www.](http://www.britastro.org/jupiter/2010report08.htm)  
1371 [britastro.org/jupiter/2010report08.htm](http://www.britastro.org/jupiter/2010report08.htm).
- 1372 Rogers, J.H., Mettig, H.J., Cidadão, A., Clay Sherrod, P., Peach, D., 2006.  
1373 Merging circulations on Jupiter: Observed differences between cyclonic and  
1374 anticyclonic mergers. *Icarus* 185, 244 – 257. doi:[10.1016/j.icarus.2006.](https://doi.org/10.1016/j.icarus.2006.05.022)  
1375 [05.022](https://doi.org/10.1016/j.icarus.2006.05.022).
- 1376 Rostami, M., Zeitlin, V., Spiga, A., 2017. On the dynamical nature of Saturn's  
1377 North Polar hexagon. *Icarus* 297, 59–70. doi:[10.1016/j.icarus.2017.06.](https://doi.org/10.1016/j.icarus.2017.06.006)  
1378 [006](https://doi.org/10.1016/j.icarus.2017.06.006).
- 1379 Rothman, L.S., Gordon, I.E., Babikov, Y., Barbe, A., Chris Benner, D.,  
1380 Bernath, P.F., Birk, M., Bizzocchi, L., Boudon, V., Brown, L.R., Campar-  
1381 gue, A., Chance, K., Cohen, E.A., Coudert, L.H., Devi, V.M., Drouin, B.J.,  
1382 Fayt, A., Flaud, J.M., Gamache, R.R., Harrison, J.J., Hartmann, J.M., Hill,  
1383 C., Hodges, J.T., Jacquemart, D., Jolly, A., Lamouroux, J., Le Roy, R.J.,  
1384 Li, G., Long, D.A., Lyulin, O.M., Mackie, C.J., Massie, S.T., Mikhailenko,

- 1385 S., Müller, H.S.P., Naumenko, O.V., Nikitin, A.V., Orphal, J., Perevalov,  
1386 V., Perrin, A., Polovtseva, E.R., Richard, C., Smith, M.A.H., Starikova, E.,  
1387 Sung, K., Tashkun, S., Tennyson, J., Toon, G.C., Tyuterev, V.G., Wagner,  
1388 G., 2013. The HITRAN2012 molecular spectroscopic database. *J. Quant.*  
1389 *Spectro. Rad. Trans.* 130, 4–50. doi:[10.1016/j.jqsrt.2013.07.002](https://doi.org/10.1016/j.jqsrt.2013.07.002).
- 1390 Rudnick, D.L., 2001. On the skewness of vorticity in the upper ocean. *Geo-*  
1391 *physical Research Letters* 28, 2045–2048. doi:[10.1029/2000GL012265](https://doi.org/10.1029/2000GL012265).
- 1392 Sada, P.V., Beebe, R.F., Conrath, B.J., 1996. Comparison of the Structure  
1393 and Dynamics of Jupiter’s Great Red Spot between the Voyager 1 and 2  
1394 Encounters. *Icarus* 119, 311–335. doi:[10.1006/icar.1996.0022](https://doi.org/10.1006/icar.1996.0022).
- 1395 Sánchez-Lavega, A., Hueso, R., Pérez-Hoyos, S., Rojas, J.F., 2006. A strong  
1396 vortex in Saturn’s South Pole. *Icarus* 184, 524–531. doi:[10.1016/j.icarus.](https://doi.org/10.1016/j.icarus.2006.05.020)  
1397 [2006.05.020](https://doi.org/10.1016/j.icarus.2006.05.020).
- 1398 Sánchez-Lavega, A., Lecacheux, J., Colas, F., Laques, P., 1993. Ground-based  
1399 observations of Saturn’s North Polar Spot and Hexagon. *Science* 260, 329–  
1400 332. doi:[10.1126/science.260.5106.329](https://doi.org/10.1126/science.260.5106.329).
- 1401 Sánchez-Lavega, A., Rogers, J.H., Orton, G.S., García-Melendo, E., Legar-  
1402 reta, J., Colas, F., Dauvergne, J.L., Hueso, R., Rojas, J.F., Pérez-Hoyos,  
1403 S., Mendikoa, I., Iñurrigarro, P., Gomez-Forrellad, J.M., Momary, T.,  
1404 Hansen, C.J., Eichstaedt, G., Miles, P., Wesley, A., 2017. A planetary-  
1405 scale disturbance in the most intense Jovian atmospheric jet from Juno-  
1406 Cam and ground-based observations. *Geophys. Res. Lett.* 44, 4679–4686.  
1407 doi:[10.1002/2017GL073421](https://doi.org/10.1002/2017GL073421).
- 1408 Sánchez-Lavega, A., Rojas, J.F., Acarreta, J.R., Lecacheux, J., Colas, F., Sada,  
1409 P.V., 1997. New Observations and Studies of Saturn’s Long-Lived North Polar  
1410 Spot. *Icarus* 128, 322–334. doi:[10.1006/icar.1997.5761](https://doi.org/10.1006/icar.1997.5761).
- 1411 Sánchez-Lavega, A., Rojas, J.F., Sada, P.V., 2000. Saturn’s Zonal Winds at  
1412 Cloud Level. *Icarus* 147, 405–420. doi:[10.1006/icar.2000.6449](https://doi.org/10.1006/icar.2000.6449).

- 1413 Sayanagi, K.M., Blalock, J.J., Dyudina, U.A., Ewald, S.P., Ingersoll, A.P., 2017.  
1414 Cassini ISS observation of Saturn's north polar vortex and comparison to the  
1415 south polar vortex. *Icarus* 285, 68–82. doi:[10.1016/j.icarus.2016.12.011](https://doi.org/10.1016/j.icarus.2016.12.011).
- 1416 Sayanagi, K.M., Dyudina, U.A., Ewald, S.P., Muro, G.D., Ingersoll, A.P., 2014.  
1417 Cassini ISS observation of Saturn's String of Pearls. *Icarus* 229, 170–180.  
1418 doi:[10.1016/j.icarus.2013.10.032](https://doi.org/10.1016/j.icarus.2013.10.032).
- 1419 Scarica, P., Grassi, D., Mura, A., Adriani, A., Ingersoll, A., Li, C., Piccioni, G.,  
1420 Sindoni, G., Moriconi, M.L., Plainaki, C., Altieri, F., Cicchetti, A., Dinelli,  
1421 B.M., Filacchione, G., Migliorini, A., Noschese, R., Sordini, R., Stefani, S.,  
1422 Tosi, F., Turrini, D., 2022. Stability of the Jupiter Southern Polar Vortices In-  
1423 spected Through Vorticity Using Juno/JIRAM Data. *Journal of Geophysical*  
1424 *Research: Planets* 127, e2021JE007159. doi:[10.1029/2021JE007159](https://doi.org/10.1029/2021JE007159).
- 1425 Scherbina, A.Y., D'Asaro, E.A., Lee, C.M., Klymak, J.M., Molemaker, M.J.,  
1426 McWilliams, J.C., 2013. Statistics of vertical vorticity, divergence, and strain  
1427 in a developed submesoscale turbulence field. *Geophysical Research Letters*  
1428 40, 4706–4711. doi:[10.1002/grl.50919](https://doi.org/10.1002/grl.50919).
- 1429 Schneider, T., Liu, J., 2009. Formation of Jets and Equatorial Superrotation  
1430 on Jupiter. *Journal of the Atmospheric Sciences* 66, 579 – 601. doi:[10.1175/  
1431 2008JAS2798.1](https://doi.org/10.1175/2008JAS2798.1).
- 1432 Scott, R.K., 2011. Polar accumulation of cyclonic vorticity. *Geophysical &*  
1433 *Astrophysical Fluid Dynamics* 105, 409–420. doi:[10.1080/03091929.2010.  
1434 509927](https://doi.org/10.1080/03091929.2010.509927).
- 1435 Shakespeare, C.J., 2016. Curved density fronts: Cyclogeostrophic adjustment  
1436 and frontogenesis. *Journal of Physical Oceanography* 46, 3193 – 3207. doi:[10.  
1437 1175/JPO-D-16-0137.1](https://doi.org/10.1175/JPO-D-16-0137.1).
- 1438 Sharma, H., Shrivastava, M., Singh, B., 2023. Physics informed deep neural net-  
1439 work embedded in a chemical transport model for the amazon rainforest. *npj*  
1440 *Climate and Atmospheric Science* 6, 28. doi:[10.1038/s41612-023-00353-y](https://doi.org/10.1038/s41612-023-00353-y).



- 1441 Showman, A.P., 2007. Numerical Simulations of Forced Shallow-Water Tur-  
1442 bulence: Effects of Moist Convection on the Large-Scale Circulation of  
1443 Jupiter and Saturn. *Journal of the Atmospheric Sciences* 64, 3132 – 3157.  
1444 doi:[10.1175/JAS4007.1](https://doi.org/10.1175/JAS4007.1).
- 1445 Siegelman, L., Klein, P., Ingersoll, A.P., Ewald, S.P., Young, W.R., Bracco, A.,  
1446 Mura, A., Adriani, A., Grassi, D., Plainaki, C., Sindoni, G., 2022a. Moist  
1447 convection drives an upscale energy transfer at jovian high latitudes. *Nature*  
1448 *Physics* 18, 357–361. doi:[10.1038/s41567-021-01458-y](https://doi.org/10.1038/s41567-021-01458-y).
- 1449 Siegelman, L., Young, W.R., Ingersoll, A.P., 2022b. Polar vortex crystals: Emer-  
1450 gence and structure. *Proceedings of the National Academy of Sciences* 119,  
1451 e2120486119. doi:[10.1073/pnas.2120486119](https://doi.org/10.1073/pnas.2120486119).
- 1452 Simon-Miller, A.A., Gierasch, P.J., Beebe, R.F., Conrath, B., Flasar, F.M.,  
1453 Achterberg, R.K., the Cassini CIRS Team, 2002. New Observational Results  
1454 Concerning Jupiter’s Great Red Spot. *Icarus* 158, 249–266. doi:[10.1006/  
1455 icar.2002.6867](https://doi.org/10.1006/icar.2002.6867).
- 1456 Smith, B.A., Soderblom, L., Batson, R., Bridges, P., Inge, J., Masursky, H.,  
1457 Shoemaker, E., Beebe, R., Boyce, J., Briggs, G., Bunker, A., Collins, S.A.,  
1458 Hansen, C.J., Johnson, T.V., Mitchell, J.L., Terrile, R.J., Cook II, A.F.,  
1459 Cuzzi, J., Pollack, J.B., Danielson, G.E., Ingersoll, A.P., Davies, M.E., Hunt,  
1460 G.E., Morrison, D., Owen, T., Sagan, C., Veverka, J., Strom, R., Suomi, V.E.,  
1461 1982. A new look at the Saturn system - The Voyager 2 images. *Science* 215,  
1462 504–537. doi:[10.1126/science.215.4532.504](https://doi.org/10.1126/science.215.4532.504).
- 1463 Smith, B.A., Soderblom, L., Beebe, R.F., Boyce, J.M., Briggs, G., Bunker, A.,  
1464 Collins, S.A., Hansen, C., Johnson, T.V., Mitchell, J.L., Terrile, R.J., Carr,  
1465 M.H., Cook, A.F., Cuzzi, J.N., Pollack, J.B., Danielson, G.E., Ingersoll, A.P.,  
1466 Davies, M.E., Hunt, G.E., Masursky, H., Shoemaker, E.M., Morrison, D.,  
1467 Owen, T., Sagan, C., Veverka, J., Strom, R., Suomi, V.E., 1981. Encounter  
1468 with Saturn - Voyager 1 imaging science results. *Science* 212, 163–191. doi:[10.  
1469 1126/science.212.4491.163](https://doi.org/10.1126/science.212.4491.163).

- 1470 Smith, B.A., Soderblom, L.A., Banfield, D., Barnet, C., Basilevsky, A.T.,  
1471 Beebe, R.F., Bollinger, K., Boyce, J.M., Brahic, A., Briggs, G.A., Brown,  
1472 R.H., Chyba, C., Collins, S.A., Colvin, T., Cook, II, A.F., Crisp, D., Croft,  
1473 S.K., Cruikshank, D., Cuzzi, J.N., Danielson, G.E., Davies, M.E., De Jong,  
1474 E., Dones, L., Godfrey, D., Goguen, J., Grenier, I., Haemmerle, V.R., Ham-  
1475 mel, H., Hansen, C.J., Helfenstein, C.P., Howell, C., Hunt, G.E., Inger-  
1476 soll, A.P., Johnson, T.V., Kargel, J., Kirk, R., Kuehn, D.I., Limaye, S.,  
1477 Masursky, H., McEwen, A., Morrison, D., Owen, T., Owen, W., Pollack,  
1478 J.B., Porco, C.C., Rages, K., Rogers, P., Rudy, D., Sagan, C., Schwartz,  
1479 J., Shoemaker, E.M., Showalter, M., Sicardy, B., Simonelli, D., Spencer, J.,  
1480 Sromovsky, L.A., Stoker, C., Strom, R.G., Suomi, V.E., Synott, S.P., Ter-  
1481 rible, R.J., Thomas, P., Thompson, W.R., Verbiscer, A., Veverka, J., 1989.  
1482 Voyager 2 at Neptune - Imaging science results. *Science* 246, 1422–1449.  
1483 doi:[10.1126/science.246.4936.1422](https://doi.org/10.1126/science.246.4936.1422).
- 1484 Smith, B.A., Soderblom, L.A., Johnson, T.V., Ingersoll, A.P., Collins, S.A.,  
1485 Shoemaker, E.M., Hunt, G.E., Masursky, H., Carr, M.H., Davies, M.E., Cook,  
1486 A.F., Boyce, J., Danielson, G.E., Owen, T., Sagan, C., Beebe, R.F., Veverka,  
1487 J., Strom, R.G., McCauley, J.F., Morrison, D., Briggs, G.A., Suomi, V.E.,  
1488 1979. The Jupiter system through the eyes of Voyager 1. *Science* 204, 951–957.  
1489 doi:[10.1126/science.204.4396.951](https://doi.org/10.1126/science.204.4396.951).
- 1490 Spiga, A., Guerlet, S., Millour, E., Indurain, M., Meurdesoif, Y., Cabanes, S.,  
1491 Dubos, T., Leconte, J., Boissinot, A., Lebonnois, S., Sylvestre, M., Fouchet,  
1492 T., 2020. Global climate modeling of Saturn’s atmosphere. Part II: Multi-  
1493 annual high-resolution dynamical simulations. *Icarus* 335, 113377. doi:[10.](https://doi.org/10.1016/j.icarus.2019.07.011)  
1494 [1016/j.icarus.2019.07.011](https://doi.org/10.1016/j.icarus.2019.07.011).
- 1495 Sromovsky, L.A., Baines, K.H., Fry, P.M., 2018. Models of bright storm  
1496 clouds and related dark ovals in Saturn’s Storm Alley as constrained by 2008  
1497 Cassini/VIMS spectra. *Icarus* 302, 360–385. doi:[10.1016/j.icarus.2017.](https://doi.org/10.1016/j.icarus.2017.11.027)  
1498 [11.027](https://doi.org/10.1016/j.icarus.2017.11.027).

- 1499 Sromovsky, L.A., Fry, P.M., Hammel, H.B., de Pater, I., Rages, K.A., 2012.  
1500 Post-equinox dynamics and polar cloud structure on Uranus. *Icarus* 220,  
1501 694–712. doi:[10.1016/j.icarus.2012.05.029](https://doi.org/10.1016/j.icarus.2012.05.029).
- 1502 Sromovsky, L.A., Limaye, S.S., Fry, P.M., 1993. Dynamics of Neptune's Major  
1503 Cloud Features. *Icarus* 105, 110–141. doi:[10.1006/icar.1993.1114](https://doi.org/10.1006/icar.1993.1114).
- 1504 Tabataba-Vakili, F., Rogers, J.H., Eichstädt, G., Orton, G.S., Hansen, C.J.,  
1505 Momary, T.W., Sinclair, J.A., Giles, R.S., Caplinger, M.A., Ravine, M.A.,  
1506 Bolton, S.J., 2020. Long-term tracking of circumpolar cyclones on Jupiter  
1507 from polar observations with JunoCam. *Icarus* 335, 113405. doi:[10.1016/j.  
1508 icarus.2019.113405](https://doi.org/10.1016/j.icarus.2019.113405).
- 1509 Trammell, H.J., Li, L., Jiang, X., Pan, Y., Smith, M.A., Bering III, E.A., Hörst,  
1510 S.M., Vasavada, A.R., Ingersoll, A.P., Janssen, M.A., West, R.A., Porco,  
1511 C.C., Li, C., Simon, A.A., Baines, K.H., 2016. Vortices in Saturn's Northern  
1512 Hemisphere (2008-2015) Observed by Cassini ISS: Vortices in Saturn's NH  
1513 from Cassini ISS. *Journal of Geophysical Research: Planets* 121, 1814–1826.  
1514 doi:[10.1002/2016JE005122](https://doi.org/10.1002/2016JE005122).
- 1515 Trammell, H.J., Li, L., Jiang, X., Smith, M., Hörst, S., Vasavada, A., 2014. The  
1516 global vortex analysis of Jupiter and Saturn based on Cassini Imaging Science  
1517 Subsystem. *Icarus* 242, 122–129. doi:[10.1016/j.icarus.2014.07.019](https://doi.org/10.1016/j.icarus.2014.07.019).
- 1518 Vasavada, A.R., Hörst, S.M., Kennedy, M.R., Ingersoll, A.P., Porco, C.C., Del  
1519 Genio, A.D., West, R.A., 2006. Cassini imaging of Saturn: Southern hemi-  
1520 sphere winds and vortices. *Journal of Geophysical Research* 111, E05004.  
1521 doi:[10.1029/2005JE002563](https://doi.org/10.1029/2005JE002563).
- 1522 Vasavada, A.R., Ingersoll, A.P., Banfield, D., Bell, M., Gierasch, P.J., Belton,  
1523 M.J.S., Orton, G.S., Klaasen, K.P., Dejong, E., Breneman, H.H., Jones, T.J.,  
1524 Kaufman, J.M., Magee, K.P., Senske, D.A., 1998. Galileo Imaging of Jupiter's  
1525 Atmosphere: The Great Red Spot, Equatorial Region, and White Ovals.  
1526 *Icarus* 135, 265–275. doi:[10.1006/icar.1998.5984](https://doi.org/10.1006/icar.1998.5984).

- 1527 Vasavada, A.R., Showman, A.P., 2005. Jovian atmospheric dynamics: an update  
1528 after Galileo and Cassini. *Reports on Progress in Physics* 68, 1935–1996.  
1529 doi:[10.1088/0034-4885/68/8/R06](https://doi.org/10.1088/0034-4885/68/8/R06).
- 1530 Verma, Y., Heinonen, M., Garg, V., 2024. ClimODE: Climate and weather  
1531 forecasting with physics-informed neural ODEs, in: *The Twelfth International*  
1532 *Conference on Learning Representations*. [arXiv:2404.10024](https://arxiv.org/abs/2404.10024).
- 1533 Weiss, J., 1991. The dynamics of enstrophy transfer in two-dimensional hydro-  
1534 dynamics. *Physica D* 48, 273–294. doi:[10.1016/0167-2789\(91\)90088-Q](https://doi.org/10.1016/0167-2789(91)90088-Q).
- 1535 Williams, G.P., Yamagata, T., 1984. Geostrophic regimes, intermediate solitary  
1536 vortices and jovian eddies. *Journal of Atmospheric Sciences* 41, 453 – 478.  
1537 doi:[10.1175/1520-0469\(1984\)041<0453:GRISVA>2.0.CO;2](https://doi.org/10.1175/1520-0469(1984)041<0453:GRISVA>2.0.CO;2).
- 1538 Wong, M.H., Simon, A.A., Tollefson, J.W., de Pater, I., Barnett, M.N., Hsu,  
1539 A.I., Stephens, A.W., Orton, G.S., Fleming, S.W., Goullaud, C., Januszewski,  
1540 W., Roman, A., Bjoraker, G.L., Atreya, S.K., Adriani, A., Fletcher, L.N.,  
1541 2020. High-resolution UV/Optical/IR Imaging of Jupiter in 2016–2019. *The*  
1542 *Astrophysical Journal Supplement Series* 247, 58. doi:[10.3847/1538-4365/](https://doi.org/10.3847/1538-4365/ab775f)  
1543 [ab775f](https://doi.org/10.3847/1538-4365/ab775f).
- 1544 Yano, J.I., Talagrand, O., Drossart, P., 2005. Deep two-dimensional turbu-  
1545 lence: An idealized model for atmospheric jets of the giant outer planets.  
1546 *Geophysical & Astrophysical Fluid Dynamics* 99, 137–150. doi:[10.1080/](https://doi.org/10.1080/03091920412331336398)  
1547 [03091920412331336398](https://doi.org/10.1080/03091920412331336398).
- 1548 Zhou, Y., Zhan, R., Wang, Y., Chen, P., Tan, Z., Xie, Z., Nie, X., 2024. A  
1549 physics-informed deep-learning intensity prediction scheme for tropical cy-  
1550 clones over the western north pacific. *Advances in Atmospheric Sciences* 41,  
1551 1391–1402. doi:[10.1007/s00376-024-3282-z](https://doi.org/10.1007/s00376-024-3282-z).

- 
- New insights on large-scale vortices in multi-year global circulation model of Saturn.
  - Comparison of vortex detection methods: GIS, neural network, and dynamical algorithm.
  - Spatial, temporal, and dynamical distributions consistent with giant planet vortices.

**Declaration of interests**

The authors declare that they have no known competing financial interests or personal relationships that could have appeared to influence the work reported in this paper.

The author is an Editorial Board Member/Editor-in-Chief/Associate Editor/Guest Editor for *[Journal name]* and was not involved in the editorial review or the decision to publish this article.

The authors declare the following financial interests/personal relationships which may be considered as potential competing interests:

Journal Pre-proof